

Theory and applications of attosecond transient absorption spectroscopy: From atoms to solids

Ennan Cui and Difa Ye(叶地发)

Citation: Chin. Phys. B, 2025, 34 (**7**): 073201. DOI: 10.1088/1674-1056/add1ba
http://cpb.iphy.ac.cn; http://iopscience.iop.org/cpb

What follows is a list of articles you may be interested in

Effect of orbital symmetry on atomic ionization in near-infrared laser fields

Manqi Xu(徐嫚琦), Shilin Hu(胡师林), Li Guo(郭丽), and Jing Chen(陈京)
Chin. Phys. B, 2025, 34 (**1**): 013202. DOI: 10.1088/1674-1056/ad8dbe

Saturated absorption spectrum of cesium micrometric-thin cell with suppressed crossover spectral lines

Junlong Han(韩俊龙), Bowen Wang(王博闻), Junhe Zheng(郑俊鹤), Shuyuan Chen(陈书源),Wei Xiao(肖伟), Teng Wu(吴腾), Hong Guo(郭弘), and Xiang Peng(彭翔)
Chin. Phys. B, 2023, 32 (**7**): 073201. DOI: 10.1088/1674-1056/acc802

High-performance coherent population trapping clock based on laser-cooled atoms

Xiaochi Liu(刘小赤), Ning Ru(茹宁), Junyi Duan(段俊毅), Peter Yun(云恩学), Minghao Yao(姚明昊), and Jifeng Qu(屈继峰)
Chin. Phys. B, 2022, 31 (**4**): 043201. DOI: 10.1088/1674-1056/ac2d21

Strong-field response time and its implications on attosecond measurement

Chao Chen(陈超), Jiayin Che(车佳殷), Xuejiao Xie(谢雪娇), Shang Wang(王赏), Guoguo Xin(辛国国), and Yanjun Chen(陈彦军)
Chin. Phys. B, 2022, 31 (**3**): 033201. DOI: 10.1088/1674-1056/ac29ab

Precision measurements with cold atoms and trapped ions

Qiuxin Zhang(张球新), Yirong Wang(王艺蓉), Chenhao Zhu(朱晨昊), Yuxin Wang(王玉欣), Xiang Zhang(张翔), Kuiyi Gao(高奎意), Wei Zhang(张威)
Chin. Phys. B, 2020, 29 (**9**): 093203. DOI: 10.1088/1674-1056/aba9c6

TOPICAL REVIEW — Ultrafast physics in atomic, molecular and optical systems

Theory and applications of attosecond transient absorption spectroscopy: From atoms to solids

Ennan Cui[1,2] and Difa Ye(叶地发)[1,†]

[1] *National Key Laboratory of Computational Physics, Institute of Applied Physics and Computational Mathematics, Beijing* 100088, *China*
[2] *Graduate School, China Academy of Engineering Physics, Beijing* 100193, *China*

(Received 3 March 2025; revised manuscript received 22 April 2025; accepted manuscript online 29 April 2025)

This review comprehensively explores the theory and applications of attosecond transient absorption spectroscopy (ATAS) in studying ultrafast electronic dynamics across various systems, from atoms to solids. Driven by significant advancements in ultrafast laser technology, such as generating isolated attosecond pulses, ATAS enables detailed investigations of ultrafast electronic processes with unprecedented time resolution. The article introduces the fundamental principles and historical development of ATAS. Applications of ATAS are discussed in three main domains: in atoms, where it has been used to study build-up dynamics of Autler–Townes splitting, Fano resonance, light-induced states, etc.; in molecules, where it has revealed coherent molecular wavepacket dynamics and non-adiabatic dynamics near conical intersections; and in solids, where it has been extended to investigate ultrafast charge carrier dynamics in metals, semiconductors, and insulators. The review highlights the potential of ATAS in developing ultrafast optical switches and petahertz electronics. The ability of ATAS to probe and manipulate electronic dynamics at the attosecond timescale provides a powerful tool for exploring the fundamental limits of electronic and optical processes in materials.

Keywords: attosecond transient absorption spectroscopy, response time, causality, petahertz electronics

PACS: 32.30.–r, 33.20.Xx, 32.80.–t, 31.15.A–

DOI: 10.1088/1674-1056/add1ba **CSTR:** 32038.14.CPB.add1ba

1. Introduction

Physicists have a penchant for exploring the limits of things, as exemplified by their continuous pursuit of lasers with ever-shorter pulse duration and ever-greater peak intensity. A milestone in this endeavor was the development of chirped pulse amplification,[1] which was awarded the Nobel Prize in Physics in 2018.[2,3] In 2001, the generation of attosecond (1 as $= 10^{-18}$ s) pulse trains (APT) through high harmonic generation (HHG) in argon gas driven by strong laser fields marked another significant advancement.[4] For APT, the limited time interval between two neighboring bursts, about 1.35 femtoseconds (1 fs $= 10^{-15}$ s), still restricted some applications in ultrafast science. The breakthrough came with the generation of isolated attosecond pulses with a duration of 650 as.[5] The advent of these attosecond pulse techniques enabled the transfer of ultrafast measurement techniques from the femtosecond to the attosecond regime, opening new avenues for various applications and leading to the emergence of attosecond science, a thriving field today.[6] The researchers involved in generating attosecond pulses were recognized with the Nobel Prize in Physics in 2023.[7–9]

Attosecond pulses have reached the timescale of electron motion around a nucleus, making them ideal for studying time-resolved atomic/molecular ionization and the subsequent physical processes. Owing to the availability of attosecond light sources, the traditional femtosecond pump-femtosecond probe spectroscopy can be naturally extended to the femtosecond-second pump-attosecond-probe spectroscopy, where the pump and probe do not overlap in the frequency domain. Attosecond transient absorption spectroscopy (ATAS), as an important complementary approach to attosecond electron/ion pump–probe spectroscopy, uses an attosecond probe pulse (typically in the extreme-ultraviolet (XUV) range, denoted by ω_{XUV}) to observe the ultrafast dynamics induced by the other delayed femtosecond pump pulse (usually in the visible (VIS) and infrared (IR) range, denoted as ω_{IR} for simplicity) by means of the absorption measurement. Absorption naturally links reflection and transmission, corresponding to attosecond transient reflection spectroscopy (ATRS) and attosecond transient transmission spectroscopy (ATTS), respectively. ATAS along with both, having a time resolution of six orders of magnitude higher than that of the state-of-the-art electronic methods and also owing to the relatively simple and easy-to-implement all-optical experimental setup, is an excellent tool for probing coherent electronic dynamics within materials. During the past 15 years or so, fruitful research results have emerged in atoms, molecules, and solids, as documented in a series of representative reviews.[10–18] Here, we will pay special attention to some

†Corresponding author. E-mail: ye_difa@iapcm.ac.cn

© 2025 Chinese Physical Society and IOP Publishing Ltd. All rights, including for text and data mining, AI training, and similar technologies, are reserved.

timing- (clocking-) related topics in ATAS that were not focused on specifically in the existing reviews. Research on time in atomic systems includes buildup time and causality. That in molecular systems addresses phenomena beyond the adiabatic approximation, particularly in the vicinity of a conical intersection (CI) and involving both adiabatic and nonadiabatic dynamics, the latter being related to electron–nuclear coupling. That in solid systems encompasses petahertz (PHz) electronics associated with the intra- and/or inter-band motion of an electron. The above topics constitute the core framework of this article.

This article is structured as follows. Section 1 provides an introduction to the topic. Section 2 is about the fundamental principles of ATAS. Sections 3–5 then detail the progress of ATAS in atoms, molecules, and solids, respectively. Finally, Section 6 offers an outlook on future perspectives.

2. Fundamental principles of ATAS

We consider the matter occupying a volume V as a unit substance which may contain single or multiple, identical or different particles. The total Hamiltonian $\hat{H}$ describing the interaction between this unit substance and the laser field under the electric dipole approximation and in the length gauge satisfies the time-dependent Schrödinger equation (TDSE)

$$\mathrm{i}\hbar\frac{\partial}{\partial t}|\psi\rangle = \hat{H}|\psi\rangle = \left[\hat{H}_{\text{matter}} - \hat{\boldsymbol{d}}\cdot\mathcal{E}(t,t_{\text{d}})\right]|\psi\rangle, \tag{1}$$

where $\hat{H}_{\text{matter}}$ and $\hat{\boldsymbol{d}}$ represent the intrinsic Hamiltonian and total dipole moment of the unit substance (which can be atoms, molecules, or solids), respectively. $\mathcal{E}(t,t_{\text{d}})$ is the two-color electric field with a time delay t_{d} between the pump and probe fields, and thus $|\psi\rangle$ is actually dependent on both t and t_{d}. Due to the conservation of total energy in the matter+field system, the energy gained (or lost) by the unit substance from the field at the end of the field (referred to as the exchanged energy) is

$$\begin{aligned}\Delta E(+\infty,t_{\text{d}}) &= \int_{-\infty}^{+\infty}\frac{\mathrm{d}}{\mathrm{d}t}\langle\psi|\hat{H}|\psi\rangle\,\mathrm{d}t \\ &= \int_{-\infty}^{+\infty}\boldsymbol{d}(t,t_{\text{d}})\cdot\frac{\partial\mathcal{E}(t,t_{\text{d}})}{\partial t}\mathrm{d}t,\end{aligned} \tag{2}$$

where $\boldsymbol{d}(t,t_{\text{d}}) = \langle\psi|\hat{\boldsymbol{d}}|\psi\rangle$. Expanding the total wave function $|\psi\rangle$ in terms of the eigenstates $|\phi_n\rangle$ of $\hat{H}_{\text{matter}}$, which are a normalized orthogonal complete basis set, that is, $|\psi\rangle = \sum_n c_n(t,t_{\text{d}})|\phi_n\rangle$, we obtain $\boldsymbol{d}(t,t_{\text{d}}) = \mathrm{Tr}[\hat{\boldsymbol{d}}\hat{\rho}(t,t_{\text{d}})]$, where the density operator $\hat{\rho} = |\psi\rangle\langle\psi| = \sum_{m,n}\rho_{mn}|\phi_m\rangle\langle\phi_n|$ with density matrix element $\rho_{mn} = c_m c_n^*$. After applying Fourier transformation and performing some straightforward calculations,[19] $\Delta E(+\infty,t_{\text{d}})$ can be converted to

$$\Delta E(+\infty,t_{\text{d}}) = \int_{-\infty}^{+\infty}\omega S(\omega,t_{\text{d}})\,\mathrm{d}\omega, \tag{3}$$

where $S(\omega,t_{\text{d}}) = 2\mathrm{Im}[\boldsymbol{d}(\omega,t_{\text{d}})\cdot\mathcal{E}(\omega,t_{\text{d}})]$ with $\omega > 0$. $S(\omega)$ is called the response function, with a positive (or negative) value indicating the absorption (or emission) probability per unit frequency at ω, or alternatively, the number of photons absorbed (or emitted) by the unit substance. In the pump–probe scenario of ATAS, the spectral coverage of the probe field is completely separate from that of the pump field, so in the detected spectral range,

$$S(\omega,t_{\text{d}}) = 2\mathrm{Im}\left[\boldsymbol{d}(\omega,t_{\text{d}})\cdot\mathcal{E}^*_{\text{probe}}(\omega,t_{\text{d}})\right],\quad \omega > 0. \tag{4}$$

It can be proven that $S(\omega)$ is gauge invariant.[20]

2.1. Numerical techniques for atomic systems

Theoretically and computationally, a variety of methods have been developed for calculating ATAS across different systems. For few-electron atoms (such as He[21,22] and Li[23–25]) and hydrogen molecules with fixed nuclei,[26] the most numerically accurate approach is solving the TDSE to obtain the full electronic wave function without any approximations. For a multi-electron atom interacting with ultra-short laser pulses, the corresponding Hamiltonian is

$$\hat{H} = \hat{T}_{\text{e}} + V_{\text{Coulomb}}(\boldsymbol{X}_{\boldsymbol{r}}) - \hat{\boldsymbol{d}}(\boldsymbol{X}_{\boldsymbol{r}})\cdot\mathcal{E}(t,t_{\text{d}}), \tag{5}$$

where $\hat{T}_{\text{e}} = \frac{1}{2m_{\text{e}}}\sum_{a=1}^{N}\hat{\boldsymbol{p}}_a^2$ is the total kinetic energy of N electrons with the momentum operator $\hat{\boldsymbol{p}}_a = -\mathrm{i}\hbar\nabla_{\boldsymbol{r}_a}$, $\boldsymbol{X}_{\boldsymbol{r}} = \{\boldsymbol{r}_1,\boldsymbol{r}_2,\ldots,\boldsymbol{r}_N\}$ denotes the set of the spatial coordinates of N electrons, $V_{\text{Coulomb}}(\boldsymbol{X}_{\boldsymbol{r}}) = V_{\text{e-nu}}(\boldsymbol{X}_{\boldsymbol{r}}) + V_{\text{e-e}}(\boldsymbol{X}_{\boldsymbol{r}})$ is the Coulomb potential that includes the electron–nuclear interaction

$$V_{\text{e-nu}}(\boldsymbol{X}_{\boldsymbol{r}}) = -\sum_{a=1}^{N}\frac{Ze^2}{4\pi\varepsilon_0 r_a}$$

and the electron–electron interaction

$$V_{\text{e-e}}(\boldsymbol{X}_{\boldsymbol{r}}) = \sum_{a<b}^{N}\sum_{b=1}^{N}\frac{e^2}{4\pi\varepsilon_0|\boldsymbol{r}_a - \boldsymbol{r}_b|}$$

with Z the nuclear charge and ε_0 the permittivity of vacuum, and $\hat{\boldsymbol{d}}(\boldsymbol{X}_{\boldsymbol{r}}) = -e\sum_{a=1}^{N}\boldsymbol{r}_a$.

However, for multi-electron atoms, the computational power of current supercomputers is insufficient to support full-electron TDSE calculations within a reasonable timeframe. To reduce computational costs, an efficient and time-saving method that retains key physical insights is the single active electron (SAE) approximation, which employs an effective model potential $V_{\text{eff}}(\boldsymbol{r})$, to describe electron–nucleus and electron–electron interactions.[27–32] In this case, the Hamiltonian of the bare atom is cast into the form $\hat{H}_{\text{matter}}(\boldsymbol{r}) = -\frac{\hbar^2\nabla_{\boldsymbol{r}}^2}{2m_{\text{e}}} + V_{\text{eff}}(\boldsymbol{r})$. Alternatively, one can also capture the essential physics by focusing on a few resonant energy levels near the light field frequency, as exemplified by the successes of few-level calculations in the context of ATAS.[33–39]

2.2. Numerical techniques for molecular systems

For tracking the time evolution of molecular structures using ATAS, particularly in ultrafast photochemical reactions, transition states, and photodissociation dynamics at conical intersections, nuclear motion must be considered, so the starting point for the total Hamiltonian is as follows:

$$\begin{aligned}\hat{H} &= \hat{T}_{\text{nu}} + \hat{T}_{\text{e}} + V_{\text{nu-nu}}(\boldsymbol{X}_{\boldsymbol{R}}) + V_{\text{e-e}}(\boldsymbol{X}_{\boldsymbol{r}}) \\ &\quad + V_{\text{e-nu}}(\boldsymbol{X}_{\boldsymbol{r}}, \boldsymbol{X}_{\boldsymbol{R}}) - \hat{\boldsymbol{d}}(\boldsymbol{X}_{\boldsymbol{r}}, \boldsymbol{X}_{\boldsymbol{R}}) \cdot \mathcal{E}(t, t_{\text{d}}), \end{aligned} \tag{6}$$

where $\hat{T}_{\text{nu}} = \sum_{A=1}^{M} \frac{\hat{p}_A^2}{2m_A}$ is the total kinetic energy of M nuclei with momentum operator $\hat{\boldsymbol{p}}_A = -\mathrm{i}\hbar\nabla_{\boldsymbol{R}_A}$,

$$V_{\text{nu-nu}}(\boldsymbol{X}_{\boldsymbol{R}}) = \sum_{A<B}^{M} \sum_{B=1}^{M} \frac{Z_A Z_B e^2}{4\pi\varepsilon_0 |\boldsymbol{R}_A - \boldsymbol{R}_B|}$$

is the nuclear interaction potential,

$$V_{\text{e-nu}}(\boldsymbol{X}_{\boldsymbol{r}}, \boldsymbol{X}_{\boldsymbol{R}}) = -\sum_{a=1}^{N} \sum_{A=1}^{M} \frac{Z_A e^2}{4\pi\varepsilon_0 |\boldsymbol{r}_a - \boldsymbol{R}_A|}$$

is the electron–nuclear interaction, and

$$\hat{\boldsymbol{d}}(\boldsymbol{X}_{\boldsymbol{r}}, \boldsymbol{X}_{\boldsymbol{R}}) = -e\sum_{a=1}^{N} \boldsymbol{r}_a + e\sum_{A=1}^{M} Z_A \boldsymbol{R}_A$$

with the set of coordinates of M nuclei

$$\boldsymbol{X}_{\boldsymbol{R}} = \{\boldsymbol{R}_1, \boldsymbol{R}_2, \ldots, \boldsymbol{R}_M\}.$$

In numerical calculations, various *ab initio* quantum chemical methods are typically employed.[40–43] The standard computational protocol involves electronic structure calculations combined with non-adiabatic dynamics simulations. These methods enable real-time tracking of electronic structure changes in molecules through ATA spectrograms, providing detailed insights into state-resolved ultrafast dynamics.

2.3. Numerical techniques for solid systems

In solids, the calculation of $S(\omega)$ usually involves the evaluation of the density matrix ρ. Consequently, solving the TDSE in atoms translates into solving the Liouville equation in solids. In semiconductors, this method is specifically referred to as the semiconductor Bloch equations,[44–48] typically having the following form:[49]

$$\begin{aligned}\mathrm{i}\hbar\frac{\mathrm{d}\rho_{mn}^{\boldsymbol{k}}(t)}{\mathrm{d}t} &= \left(E_m^{\boldsymbol{K}(t)} - E_n^{\boldsymbol{K}(t)} - \mathrm{i}\hbar\Gamma_{mn}\right)\rho_{mn}^{\boldsymbol{k}}(t) \\ &\quad + e\mathcal{E}(t)\cdot\sum_{n'}\left[\boldsymbol{d}_{mn'}^{\boldsymbol{K}(t)}\rho_{n'n}^{\boldsymbol{k}}(t) - \boldsymbol{d}_{n'n}^{\boldsymbol{K}(t)}\rho_{mn'}^{\boldsymbol{k}}(t)\right], \end{aligned} \tag{7}$$

where $\boldsymbol{K}(t) = \boldsymbol{k} + e\boldsymbol{A}(t)/\hbar$, with $\boldsymbol{k}$ the crystal momentum and $\boldsymbol{A}(t) = -\int_{-\infty}^{t}\mathcal{E}(t)\mathrm{d}t$ the vector potential of the laser field, $E_m^{\boldsymbol{K}(t)}$ is the energy dispersion of the m-th band, $\boldsymbol{d}_{mn}^{\boldsymbol{K}(t)}$ is the Berry connection between different bands, and Γ_{mn} represents the phenomenological relaxation rate. The band indices m, n, and n' run over all energy bands.

Model-based methods generally rely on the mean-field approximation. For calculating the interaction of complex systems or real materials with the ultrafast laser field, first-principles methods are required. The most common method is the time-dependent density functional theory (TDDFT),[50,51] which is applicable to atoms,[52,53] molecules,[54–56] and solids.[17,47,48,57] Another method treats a solid heterojunction (electrode–material–electrode) driven by an external field as a quantum open system, utilizing first-principles quantum transport theory, where the calculation results of density functional theory serve as an input for the subsequent calculations based on non-equilibrium Green's functions, to simulate the photoinduced charge/current response of the heterojunction.[58] This method was initially applied in the semiconductor industry during its early development.

2.4. Macroscopic propagation effects

Transient absorption spectra are macroscopic observables. Thus, the single-atom/molecule approximation only provides absorption spectra for dilute samples. For media such as dense gases or thick materials with large optical thickness, it is necessary to consider the spatial propagation effects of the laser field and phase-matching processes to quantitatively explain the experimental data with theoretical calculations.[59] The general approach involves jointly and self-consistently solving the TDSE for atomic systems or the time-dependent Kohn–Sham equation for solids coupled with Maxwell's wave equation. At each discrete spatial grid point, the latter uses the polarization function obtained from the former to inversely compute the electric field at the next spatial point, while the former updates the polarization function using the newly calculated electric field.[60] This method equally takes both linear and nonlinear optical effects into consideration. Despite the pulse propagation effect, Beer's law remains a very good approximation to compute the final radiation spectrum, when the XUV pulse is sufficiently weak to ensure the validity of the linear response theory and meanwhile sufficiently short to be well modeled by a delta function.[61] In this case, Eq. (4) continues to be valid in describing the changes in optical density.

3. ATAS in atoms

ATAS was first demonstrated through the time-resolved observation of inner-atomic electron dynamics induced by ionization in Kr ions in 2010.[62] Shortly thereafter, Wang *et al.* applied ATAS to observe the autoionization dynamics of Ar initiated by an isolated attosecond pulse. They found that the measured lifetimes of the autoionized states were consistent with the values deduced from static spectroscopy.[63] Both

of these pioneering experiments were conducted on a few-femtosecond timescale. The first ATAS experiment to reveal subcycle dynamics was performed in He exposed to a moderately intense IR pulse and probed by an attosecond pulse train.[64]

Since then, He atoms have garnered sustained attention as a gas target system and have become a focal point of research. As the simplest multi-electron atom, He allows for full-dimensional TDSE calculations to be solved exactly with current computing power resources. This characteristic facilitates quantitative comparison between theoretical predictions and ATAS experimental results. As a prototypical model, the phenomena and mechanisms observed in He ATAS encompass nearly all aspects of atomic ATAS under the present investigation. Therefore, we will primarily focus on He in the following discussions. Note that atomic units are used throughout this section unless stated otherwise.

3.1. Main features in the ATAS

In 2013, complete ATA spectrograms for He were obtained under both double excitation[65] and single excitation[66] conditions, as illustrated in Figs. 1(a) and 1(b), respectively. In Fig. 1(a), a negative delay indicates that the IR/VIS pulse arrives first and the XUV pulse later. The photon energy of the pump is ~ 1.7 eV, with an intensity of 3.5×10^{12} W/cm^2. The energy difference between 2s2p and $sp_{2,3+}$ bright states is twice the pump photon energy, permitting a two-photon near-resonance transition with the $2p^2$ state acting as an intermediate dark state. All of them are autoionized states embedded in the single ionization continuum background. In Fig. 1(b), a negative delay indicates that the XUV pulse arrives before the IR pulse, which is the same as in Fig. 1(c). For the remainder of this section, the definition of delay will follow the convention established in Figs. 1(b) and 1(c).

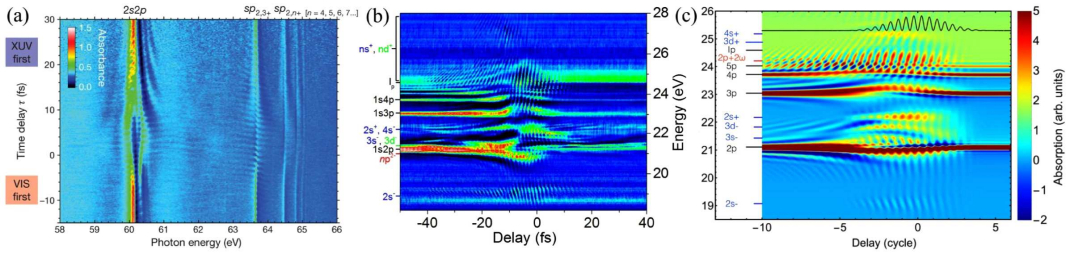


Fig. 1. Typical ATA spectrograms observed in experiment: (a) double-excited states (from Ref. [65]) and (b) single-excited states (from Ref. [66]) of the He atom, as well as (c) the full TDSE calculations for the single-excited states (from Ref. [27]). In these panels, the overlap of the peak intensities of the pump and probe pulses defines the delay as zero. In (b) and (c), a positive delay means that the pump (IR) pulse arrives before the probe (XUV) pulse. Note that the definition on the sign of the delay time is reversed in (a).

The He ATA spectrograms exhibit rich and intriguing features.

Large positive delay When the XUV and IR pulses do not overlap, and the IR pulse arrives well before the XUV pulse, the IR pulse alone is insufficient to induce the transition or ionization of He atom from its ground state. Thus, we conclude that He atoms do not exhibit a detectable response to the IR photon. The XUV pulse arriving after the IR pulse has completely vanished promotes the atom from the ground state to excited np bound states and low-energy continuum states through a single-XUV-photon transition. The induced dipole moment subsequently decays due to dephasing. Consequently, the transient absorption spectrum displays a delay-independent absorption line shape at each atomic resonance energy level, manifesting as a Lorentzian line shape for single-excited states and a Fano line shape for autoionizing states.[67]

Actually, ATAS can be classified as a two-color pump–probe ultrafast spectroscopy technique, where the physical processes differ significantly depending on the pulse sequence. When the IR pulse arrives first, the scheme is consistent with traditional femtosecond pump–probe schemes. In the context of strong-field ionization (IR field is strong), the IR pulse first removes a valence electron by quantum tunneling and creates a vacancy in the atom, while the attosecond pulse subsequently triggers an inner-shell excitation and thus acts as a probe of the coherent electron wavepacket created by the IR pulse. Some pioneering experiments along this direction can be found, e.g., in Refs. [62,68,69]; see also Ref. [60] for a comprehensive theoretical treatment. On the other hand, when the IR pulse arrives later, the process more closely resembles a time-resolved wave-mixing effect, which can also be referred to as "perturbed free induction decay". In this review, we focus more on the second scheme.

Large negative delay If the XUV and IR pulses do not overlap but now the XUV pulse arrives well before the IR pulse, it will first promote the atom from the ground state to the excited states mentioned above. The induced dipole moment undergoes free induction decay (FID) for a period of time before being strongly perturbed by the subsequent arrival of the IR pulse. The difference among these perturbed dipoles is that the wave packets (WPs) of the excited states, despite having the same initial phase but different energies, evolve freely over the time interval between the arrival of XUV and IR pulses, accumulating different phases that are proportional

to $\omega \times t_{\rm d}$. The hyperbolic relationship $\omega \times t_{\rm d} =$ constant manifests as delay-dependent hyperbolic sidebands adjacent to the main absorption peak in the ATA spectrogram. As the negative delay increases, these sidebands move away from the center. This phenomenon, known as perturbed FID, has been extensively studied in Fourier transform nuclear magnetic resonance spectroscopy.[70,71]

Overlap region For the delay region where the XUV and IR pulses overlap, the features in the ATA spectrogram become richer and more complex, with IR light-induced states (LISs) emerging here. The first notable feature is the subcycle oscillation, most prominently observed at a frequency of $2\omega_{\rm IR}$ [Fig. 1(c)]. Notably, for the high-lying states, the subcycle oscillation persists even at large negative delays. The $2\omega_{\rm IR}$ oscillation signifies the involvement of a two-IR-photon transition.[27,29] The underlying mechanism is called quantum "which-way" interference, which typically involves two or more absorption pathways constructively or destructively interfering with each other and manifests in the delay-dependent brightness and darkness in the absorption spectrum [see Fig. 1(c)].

For a singly excited helium atom, its ground state, the 1s2p excited state, and the 1s5p excited state form a three-level system. Due to parity conservation, single photon transition between the 1s2p and 1s5p states is forbidden, while double photon transition between them is allowed. The dipole transition from the ground state to the 1s5p state via a single XUV photon at angular frequency ω_{np} forms the first absorption channel, referred to as "direct" (XUV only). The second absorption channel, referred to as "indirect" (XUV+IR+IR), arises when the atom first absorbs an XUV photon with energy ω_{2p} to transition from the ground state to the 1s2p state, followed by the absorption of two IR photons to transition to the 1s5p state in a delay-dependent manner. When interfering, two absorption channels involve different frequencies of XUV photons, resulting in a subcycle oscillation in the ATA spectrograms with an angular frequency of $\omega_{np} - \omega_{2p} = 2\omega_{\rm IR}$. In 2013, Chang's group confirmed experimentally that the subcycle oscillations observed in the bound states of laser-dressed Ne atoms were caused by quantum interference between different multiphoton excitation pathways.[72]

For the series of bright fringes in the high-lying state manifold of Fig. 1(c), further studies indicated that the constructive interference condition as a function of delay for $t_{\rm d} < 0$ is given by[27]

$$\left(\omega_{np} - \omega_{2p}\right)|t_{\rm d} - t_0| + \Delta\phi = 2\pi k, \tag{8}$$

where k is a positive integer, and the sign of the energy difference between the np and 2p states, $(\omega_{np} - \omega_{2p})$, determines the tilt direction of the interference fringes in the ATA spectrogram. For more details, see Refs. [27,30].

Subcycle oscillations arise from the contribution of the counter-rotating terms in the total light–matter Hamiltonian. When solving the TDSE under the rotating wave approximation (RWA), the resulting ATA spectrogram will not exhibit LISs, and the subcycle oscillation features are absent.[35,36] References [36,73] demonstrate this point by the TDSE calculations of a three-level model in the weak- and moderate-coupling regimes, respectively. The latter is shown in Figs. 2(a) and 2(c). It is important to note that in the weak- and moderate-coupling regimes, the RWA can accurately reproduce the main structures of the full TDSE results. In the strong-coupling regime, however, the RWA breaks down.[74]

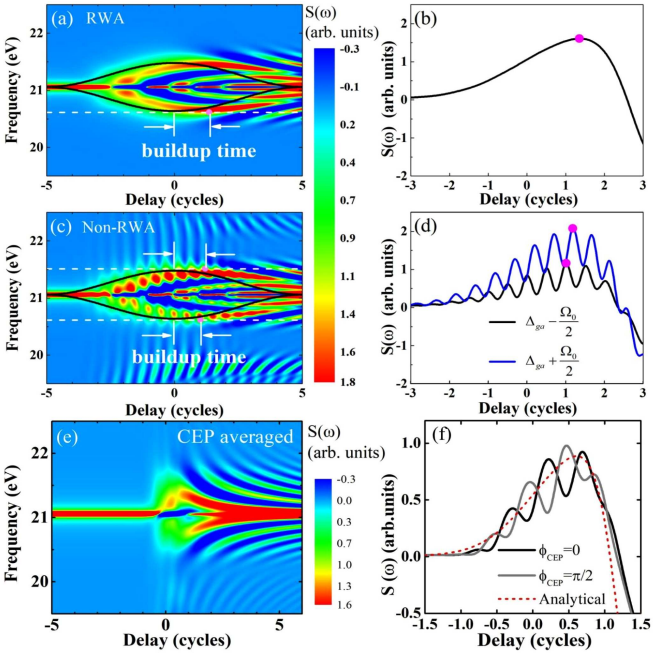


Fig. 2. ATA spectrograms are calculated based on a three-level model for He atoms, either with (a) or without (c) the RWA. The black solid lines in (a) and (c) are the instantaneous Floquet states following the envelope of the IR pulse. It is interesting to note that the maximal Autler–Townes splitting does not occur at delay zero. For clear visualization, (b) and (d) demonstrate the absorption line profile as a function of delay at the maximal Autler–Townes splitting ($\omega_{\rm AT} = \Delta_{\rm ga} \pm \Omega_0/2$) indicated by the white dashed lines in (a) and (c). (e) and (f) The corresponding results for a few-cycle ultrashort laser pulse to reveal the CEP effects. The red dashed line in (f) is obtained by Eq. (9). Adapted from Ref. [73].

In the overlap region of the XUV and IR pulses, the second notable feature of the ATA spectrogram is the emergence of a doublet structure, characterized by the splitting on either side of the main absorption peak of laser-dressed atoms. A prime example is the 1s2p singly excited state of He atoms, as illustrated in Fig. 1. This phenomenon is primarily governed by the delay-dependent Autler–Townes (AT) effect.[36,75] It can be well explained by a three-level model, which can be decoupled into two independent two-level systems.[36] According to the results of TDSE calculations for such a system, the shifted energy levels under a strong field correspond to the position of the outermost doublet in the ATA spectrogram, often referred to in some literature as the "outermost fork-like struc-

ture". When resonance occurs, the doublet splitting becomes symmetric, and both intensities are equal. This is commonly known as the AT effect, as illustrated in Figs. 2(a) and 2(c). In the case of positive detuning, the doublet splitting becomes asymmetric with the upper branch having lower intensity and being further from the main absorption peak, while the lower branch has higher intensity and is closer to the main absorption peak.[77]

When more bound states, as well as the continuum, are considered and their coupling to the 1s2p and 1s2s levels is taken into account, the AC Stark effect can cause the original symmetric splitting of an AT doublet in the resonance case to deviate from perfect symmetry, as illustrated in Fig. 3(a), which presents the full-dimensional TDSE simulations of He atoms under the SAE approximation. Specifically, when the intensity of the IR pulse is sufficiently high, the probability of ionization by the pump becomes non-negligible, resulting in a significant variation of the absorption spectrum, including observable line shape modification and absorbance reduction in the overlap region. In the case of Ar, for instance, both experiment[63] and theory[78] demonstrated that SFI can speed up the decay process of autoionization and thus modify the line shape in the ATA spectrogram.

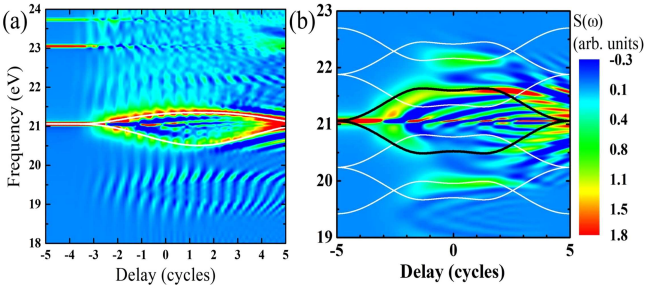


Fig. 3. (a) ATA spectrogram of He atoms obtained via numerical solution of the full-dimensional TDSE, showing that the line profile (position and asymmetry) and, specifically, the buildup time of the Autler–Townes splitting are both in good agreement with the predictions of Eqs. (9) and (10). (b) ATA spectrogram in the strong-coupling regime, where avoided crossings are found to leave footprints on the spectrum. Adapted from Ref. [73].

3.2. Buildup time of the Autler–Townes splitting

In the resonance case, it is natural to expect that the splitting of the AT doublet in the ATA spectrogram is maximized at the peak of the instantaneous pump intensity, according to the prediction of adiabatic Floquet formalism, as illustrated by the black solid lines in Figs. 2(a) and 2(c). It is important to note that the derivation of Floquet formalism employs a monochromatic field to facilitate the Fourier series expansion, while real ultrafast pulses possess a certain spectral width due to their envelope in the time domain. Thus, the black solid lines in Figs. 2(a) and 2(c) actually depict the instantaneous Floquet levels derived from a monochromatic alternating electric field with its amplitude varying with delay. Specifically, Ref. [36] provides an analytical solution to the TDSE with RWA for the interaction of a pump pulse with $\cos^2$ and $\sin^2$ envelopes with a two-level system. The calculated ATA spectrogram from this reference (see its Fig. 7) shows excellent agreement with the numerical results of the TDSE (see its Fig. 1).

Both the results of the ATAS experiments in Fig. 1 and the TDSE calculations in Fig. 2 reveal a shift along the delay axis. Specifically, the maximum of AT splitting occurs when the XUV pulse arrives before the IR pulse, which is the third feature of the ATA spectrogram in the overlap region. To clearly identify the buildup time, Figs. 2(b) and 2(d) show the profile of $S(\omega)$ at the maximum AT splitting, denoted by the white dashed lines at $\omega_{\mathrm{AT}} = \Delta_{ga} \pm \Omega_0/2$ in Figs. 2(a) and 2(c). Here, Δ_{ga} is the energy gap between an excited state $|a\rangle$, to be probed by the XUV light, and the ground state $|g\rangle$. Ω_0 is the Rabi frequency induced by the strong coupling between $|a\rangle$ and another excited state $|f\rangle$ by the IR pump field. When considering the RWA, it can be demonstrated that there is no carrier-envelope phase (CEP) effect, and the buildup times of the upper and lower branches of AT splitting are the same. However, as for the non-RWA, the buildup time becomes CEP-dependent. Even when averaging out the CEP effect, this shift remains evident. Reference [73] utilized the three-level model originally proposed in Ref. [36] mentioned above to explain these observations. Under the RWA, they first derived an exact analytical solution in the resonant case. Then, by applying the slowly varying envelope approximation and assuming an infinitely long decoherence time, they obtained an analytical expression for the delay-dependent absorption spectrum at the maximum of AT splitting as follows:

$$S(\tau) \propto \int_0^{+\infty} \cos\left(t^{*3} - 3\tau^* t^{*2} + 3\tau^{*2} t^*\right) \mathrm{d}t^*. \tag{9}$$

Finally, based on the above derivations, a scaling law for the buildup time was established

$$\tau_0 = \alpha^3 \sqrt{\frac{12}{\Omega_0 \left|\partial_{tt} \mathscr{A}(0)\right|}}, \tag{10}$$

which depends on the atomic and laser parameters encapsulated in the Rabi frequency and the curvature of the pump pulse envelope around the peak, and $\alpha = 0.654$ is a universal constant. The scaling law was later extended to the near-resonance case.[77] In Fig. 2(f), it can be seen that for the weak or moderate coupling, Eq. (9) effectively explains the CEP-averaged absorption profile, which corresponds to a CEP-not-stabilized experiment. Moreover, the CEP-averaged buildup time is also in accordance with the analytical prediction of Eq. (10) [red dashed line in Fig. 2(f)]. The white line in Fig. 3(a) represents the analytical result from Floquet theory, which incorporates corrections from the AC Stark effect and the delay displacement brought by the buildup time, matching well with the numerical result from the full TDSE (color background).

Additionally, Eq. (10) successfully explains the previously observed but unrecognized buildup time in earlier ATAS experiments and simulations, such as the AT splitting of the near-resonant doubly excited state of the He atom[79] [see Fig. 5(a)] and the core-electron excitation of the Xe atom[80] [see Fig. 5(b)].

For strong coupling, as illustrated in Fig. 3(b), the quasi-energy levels undergo significant deformation due to avoided crossing, resulting in the maximum splitting not appearing at zero delay. Thus, the buildup time in this regime cannot be as well-defined as in the low-intensity case. Nevertheless, the shift between the ATA spectrogram and the instantaneous Floquet states remains quite pronounced. If the shoulder of the spectrogram is used to define the buildup time, the value obtained is quite close to the prediction of Eq. (10)[73]

The link between buildup time and response time The real world adheres to causality, and this is reflected in the general relationship between the electric displacement and the external field, as revealed by Eq. (7.111) and (7.112) of Ref. [84]. The presence of an integral over the time interval of $[0,+\infty)$ in these equations guarantees causality but introduces a response time, which is implicit in the Green function and the dielectric function. This indicates that a material's response to an external field is non-instantaneous.[85–89] According to these equations, if a material has no response time to an external field, i.e., if the dielectric function $\varepsilon(\omega)$ is constant, then the only scenarios that would satisfy this condition would be a vacuum (since any material's dielectric function depends on frequency) or a direct current induced by a constant external electric field. Causality requires that the dielectric function $\varepsilon(\omega)$ be an analytic function of ω in the upper half-plane, leading to the well-known Kramers–Kronig relation between the real and imaginary parts of the dielectric function.[84] Due to the absorption and radiation of a material, there are absorptivity $\mathcal{A}$ obtained from $\alpha(\omega)$, refractivity $\mathcal{N}$ obtained from $n(\omega)$, and reflectivity $\mathcal{R}$ with the relation that $\mathcal{A}+\mathcal{N}+\mathcal{R}=1$ guaranteed. In principle, experimentally measuring the delay-dependent transient absorption by ATAS or transient refraction/reflection by ATRS inherently contains information about the response time.

It is essential to note that time is not an operator within the framework of quantum mechanics.[86] The characterization of response time may vary among different physical systems. In the context of ATAS, our response time refers specifically to the analysis of $\Delta S(\omega,t_{\rm d})$ detected by the XUV pulse upon the arrival of the IR pulse center.

About 40 years ago, during the era of picosecond (ps) and femtosecond lasers, ultrafast spectroscopists proposed how to calibrate the zero point of time (zero delay) in a pump–probe experiment. The standard method for calibrating zero delay is using the maximum absorption obtained from the femtosecond transient absorption spectrum. Limitations in experimental conditions and uncertainty, as well as time resolution at that time led many experimentalists to conclude that the material's response to external fields was instantaneous.[90–93] For instance, an early observation of the dynamic optical Stark shift[76] revealed that, with a time resolution of twenty femtoseconds or so, the maximum value of the dynamic shift coincided with a delay time of 0 fs, as shown in Fig. 4(a). With the advent of attosecond lasers and improvements in time resolution, it became possible to observe the electronic ultrafast coherent dynamics with sub-fs time resolution, making the detection of response time feasible. At this time, the calibration of zero delay became exceptionally important. The conventional method of assuming that maximum absorption corresponds to zero delay is no longer considered reliable, and several new methods have been proposed.[82,94] One of them, as a fully experimental method for delay-zero calibration, involves extracting the $4\omega_{\rm IR}$ oscillation from a specific high harmonic [e.g., HH13 shown in Fig. 5(d)] within the APT using IR-pump and APT-probe ATAS. By performing time-frequency wavelet analysis, the resulting spectrum [Fig. 5(d)] reveals a very stable maximum at the delay-zero for the $4\omega_{\rm IR}$ oscillation, providing a reliable and robust experimental basis for delay-zero calibration.

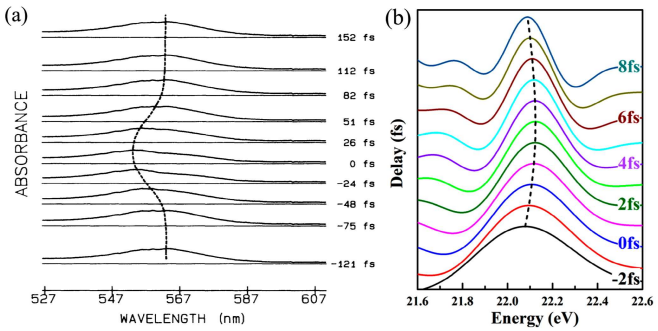


Fig. 4. A zero response time was concluded from the delay-dependent absorption spectrum obtained by a coarse femtosecond-pump–femtosecond-probe spectroscopy in the organic dye molecule rhodamine-B in solution (a), but not in a finer femtosecond-pump–attosecond-probe spectroscopy in helium atom (b). Adapted from Refs. [76,77], respectively.

In a series of ATAS experiments, it was observed that there was a significant shift between the delay corresponding to maximum AT splitting or the AC Stark shift in the ATA spectrogram and the delay-zero where the pulse peaks of the pump and probe coincided, as clearly shown in Fig. 4(b). This so called buildup time is rather general, also manifesting itself in ATAS of other systems, such as the polar LiF molecule[81] [see Fig. 5(c)] and excitons in the 0.5-mm thick magnesium oxide (MgO)[83] [see Fig. 5(e)]. It can serve as a measure of the atomic system's response time,[73] taking the envelope of the IR pulse as the hand of the clock.

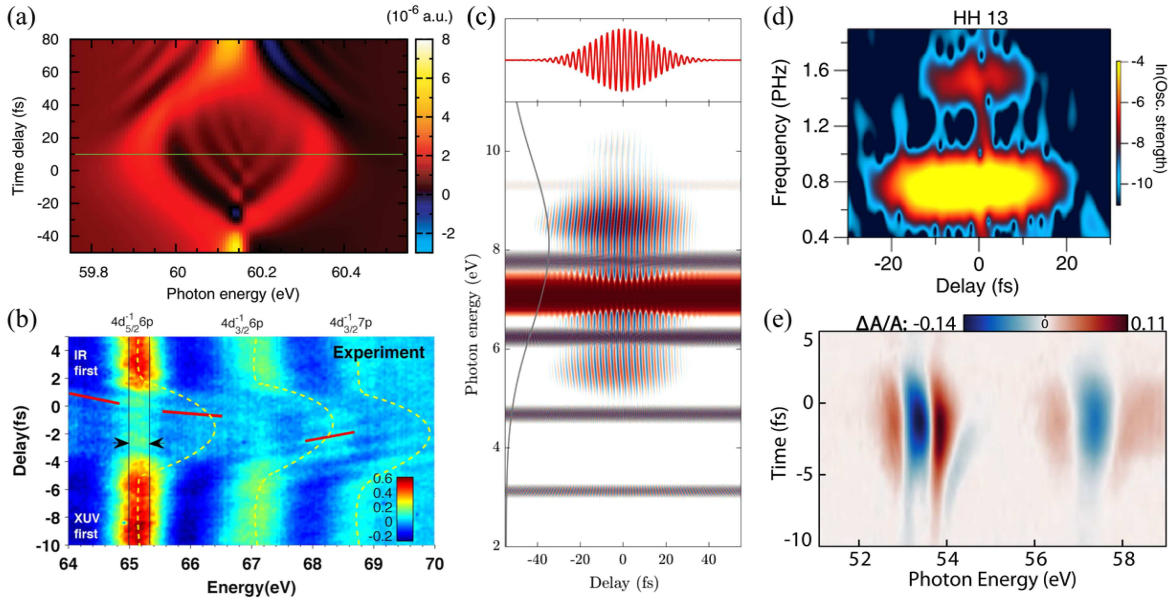


Fig. 5. Demonstration of the university of buildup times that are discernable in various systems: doubly excited states of He atom (a), core electron excitation of Xe atom (b), polar LiF molecule (c), singly excited state of He probed by APT rather than SAP (d), and excitons in 0.5-mm thick magnesium oxide (e). Panels (a)–(e) are adapted from Refs. [79–83], respectively.

3.3. Causality and the dipole reconstruction

The phase information contained in the dipole moment helps to understand the origin of quantum beat within the system. In the overlap region of ATA spectrograms, experiments have demonstrated that the near-infrared (NIR) coupling can alter the phase of the induced time-dependent dipole moment, resulting in a transformation of the spectral line shape from Fano to Lorentzian and back to Fano.[95] An analytical theoretical explanation for this phenomenon was provided based on the Fourier analysis of the real-time dipole moment.[96] Subsequently, Refs. [97,98] presented a general theory of dipole reconstruction, combined with numerical simulations, elucidating how to retrieve the time evolution of the amplitude and phase of the atomic dipole moment from the experimental observable, optical density (OD). Furthermore, it was discovered that the dipole reconstructed from ATAS can be utilized to extract information about atomic recollision in real time, eliminating the need for delay sweeping, as shown in Fig. 6.[99]

The essential idea of dipole reconstruction is as follows. In the linear response regime, the relationship between the dipole moment and the probe electric field along the linear polarization direction of the probe in the frequency domain is given by

$$d\left(\omega,t_{\mathrm{d}}\right)=\chi\left(\omega,t_{\mathrm{d}}\right)\mathcal{E}_{\mathrm{probe}}\left(\omega,t_{\mathrm{d}}\right) \tag{11}$$

with the electric susceptibility $\chi(\omega)$ representing the response function to an external impulse stimulus. In the time domain,

$$\begin{aligned} d\left(t,t_{\mathrm{d}}\right) &= \chi\left(t,t_{\mathrm{d}}\right)*\mathcal{E}_{\mathrm{probe}}\left(t,t_{\mathrm{d}}\right) \\ &= \int_{0}^{+\infty}\chi\left(t',t_{\mathrm{d}}\right)\mathcal{E}_{\mathrm{probe}}\left(t-t',t_{\mathrm{d}}\right)\mathrm{d}t', \end{aligned} \tag{12}$$

where the integration range extends from 0, rather than $-\infty$, to $+\infty$ due to the causality. It can be proven that $\chi(\omega)$ and $\sigma(\omega)$ are related as follows:[98]

$$\chi\left(t,t_{\mathrm{d}}\right)\propto\mathcal{F}^{-1}\left[-\mathrm{i}\frac{\sigma\left(\omega,t_{\mathrm{d}}\right)}{\omega}\right],\quad t>0, \tag{13}$$

where $\mathcal{F}^{-1}$ denotes the inverse Fourier transform, and we have made an even extension of the experimentally measured absorption cross section $\sigma\left(\omega,t_{\mathrm{d}}\right)$ into the negative frequency domain. As long as the optical density of the probe field, after absorption, is measured experimentally, the time- and delay-dependent dipole moment can be accurately reconstructed by Eqs. (12) and (13).

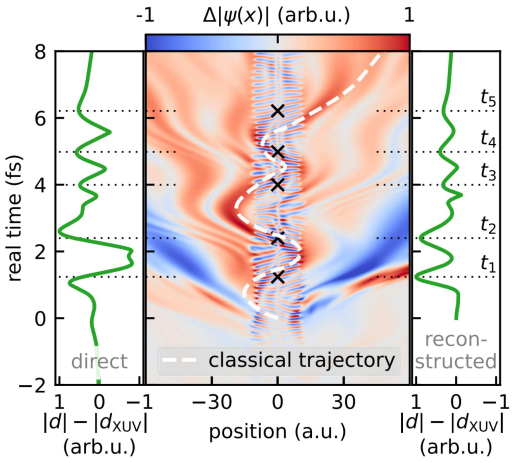


Fig. 6. Reconstructed time-dependent dipole moment (right panel) compared with the original one (left panel), revealing clear signatures of rescattering of a classical trajectory (middle panel), a cornerstone of strong-field physics and attosecond optics. Adapted from Ref. [99].

4. ATAS in molecules

Traditional nanosecond, picosecond, and femtosecond pump–probe techniques have been widely applied in ultrafast photophysics and photochemistry, typically used to observe chemical reaction dynamics, charge transfer, intra- and

inter-molecular energy transfer, as well as various relaxation processes such as electron–, exciton– or polaron–phonon coupling. These processes often involve a significant amount of incoherent information, complicating the analysis of specific dynamics. However, ATAS offers an attosecond time resolution that is much shorter than these relaxation times, enabling the observation and manipulation of the coherent dynamics of molecular WPs, an area that traditional methods have not achieved, and filling the research gap in the molecular dynamics across different time scales.

4.1. Early exploration and the study of wave packet dynamics and its reconstruction

By 2016, several groups had expanded the ATAS application to simple small molecular systems, aiming at reconstructing the WP dynamics in the time domain. A proof-of-principle experiment, using molecular hydrogen as a case study, demonstrated that ATAS could detect the electronic and nuclear wave packet (WP) dynamics with high spectral resolution (dependent on the XUV spectral resolution and width) and attosecond temporal resolution (dependent on the XUV pulse duration), and further reconstruct the nuclear WP of the electronic excited state based on this finding.[100] Subsequently, the coherent dynamics of the electronic ($2\omega_{IR}$ oscillation with a period of 2.7 fs), vibrational (oscillation period of 14.5±0.1 fs), and rotational (with molecular alignment occurring at approximately 80 fs) states of NO^+, simultaneously and comprehensively as well as in real time, on the attosecond to sub-picosecond time scale,[101] were observed and resolved for the first time by employing ATAS at the nitrogen K-edge (400 eV).[101] As a further advance, Leone's group utilized XUV transient absorption spectroscopy of molecular iodine (I_2) to map and image the one-photon-absorption induced vibrational dynamics on the $B\,^3\Pi_{0^+_u}$ state of a highly extended vibrational WP [see Fig. 7(c)], as well as the dissociation dynamics following two-photon absorption separately into the $Y\,^3\Sigma^-_{0^+_g}$ state and $Z\,^3\Pi_{0^+_g}$ state [see Fig. 7(b)].[102] Following the same idea, they also reconstructed the core-to-valence transition energy as a function of internuclear distance using the transient absorption data, as shown in Fig. 7(d).

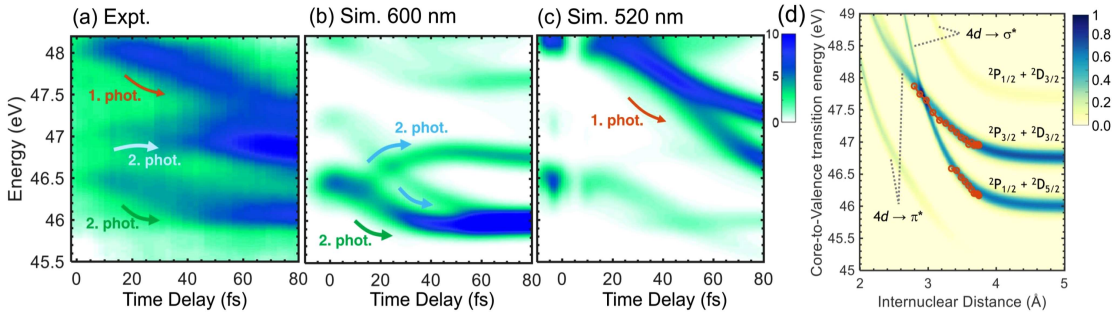


Fig. 7. Experimentally measured ATA spectrogram (a) compared with the simulated ones following 600-nm (b) and 520-nm (c) pump excitation, respectively, which help to identify the main channels underlying the spectra. The red arrow indicates the one-photon-induced vibrational dynamics on the $B\,^3\Pi_{0^+_u}$ state while the green and cyan arrows indicate the dissociation dynamics from the $Y\,^3\Sigma^-_{0^+_g}$ and $Z\,^3\Pi_{0^+_g}$ states via two-photon absorption, respectively. (d) illustrates that the experimentally extracted potential-energy curve is in good agreement with theoretical predictions. Adapted from Ref. [102].

4.2. Non-adiabatic dynamics near the conical intersection

The adiabatic approximation essentially assumes that electrons remain in an eigenstate when considering the nuclear motion, neglecting the coupling between different electronic states. However, in the chemical reaction dynamics involving the formation and breaking of the chemical bond, different adiabatic potential energy surfaces (eigenvalues of the electronic Hamiltonian) may be very close or even overlap (implying degeneracy). In such cases, it becomes necessary to consider the coupling between different electronic states which leads to non-adiabatic dynamics. Bækhøj *et al.* theoretically describe the ATAS near a conical intersection (CI) using a vibronic coupling model.[103] They categorize the non-adiabatic vibrational coupling strength into three regimes: weak, intermediate, and strong, and discuss the spectral features in the ATA spectrogram for each regime. It is important to note that, because the model assumes that the potential energy surfaces are quadratic, this model is only applicable to explaining the physics near the CI but not for the situation where the internuclear distance is significantly far from the CI, such as the photoinduced dissociation process.

In the weakly coupled system, the electronic states remain in the adiabatic eigenstates, making the Born–Oppenheimer (BO) approximation valid. Relevant studies include Ref. [26] which investigates the characteristics of hydrogen molecular ions and hydrogen molecules in both fixed nuclei and nuclear motion scenarios within the context of ATAS, and Ref. [81], which explores the influence of a non-zero permanent dipole moment on the sub-fs electronic dynamics, using the polar LiF molecule as a case study.

In the moderate and strong coupling regimes, electronic states move along harmonic potential energy surfaces, non-adiabatically passing through the CI region, making the BO approximation invalid. The emergence of attosecond lasers

has sparked a growing interest in the direct observation and manipulation of such non-adiabatic dynamics over the past decade. As a prototypical molecule for non-adiabatic photodissociation dynamics, iodine monobromide (IBr) has valence electrons that undergo both adiabatic and non-adiabatic pathways at avoided crossings and CIs after the excitation of a VIS-pump pulse, leading to the formation of various products, as shown in Fig. 8. A comparison between ATAS and *ab initio* quantum chemical simulations clearly shows the absorption features associated with the nuclear separation dynamics.[104]

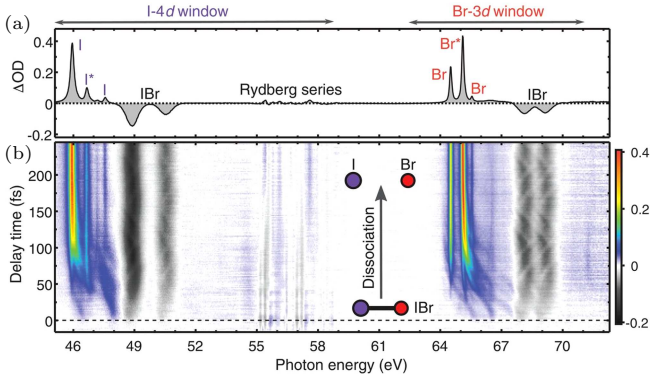


Fig. 8. Elemental and core-level resolved ATA spectrogram of IBr, demonstrating its remarkable capability in tracing the molecular dissociation process, which is triggered at the delay-zero and proceeding toward the positive delays. Adapted from Ref. [104].

As demonstrated above, the use of broadband XUV/x-ray radiation allows access to the core levels of different elements which are spectrally well-separated and element-specific, making ATAS particularly promising for tracking atto-chemistry in large molecules. Investigations employing the spectrum of the probe light covering the core electron excitation of halogen elements have been extended to organic molecules, yielding a series of significant advancements. In 2019, the complete evolution of the neutral excited-state WP in CH_3Br[105] was observed in real time, from the initial excitation through the CI to the ensuing fragmentation, which was verified by molecular WP propagation simulations. References [106–108] combine ATAS experiments with a multireference theoretical method[41] that fully simulates the UV pump-XUV/x-ray probe measurement, investigating in detail the non-adiabatic photodissociation dynamics for a series of alkyl iodide molecules with different R-group structures (CH_3I, C_2H_5I, *i*-C_3H_7I, and *t*-C_4H_9I) by probing iodine 4d core-to-valence transitions in the XUV band of 45 eV to 70 eV. Electronic state switching, that is, WP bifurcation at a CI implies charge transfer. In 2022, a soft x-ray ($\sim$ 108 eV, covering the silicon $L_{2,3}$-edge) ATAS experiment in neutral silane (SiH_4)[109] demonstrated the observation of charge migration in 690 as, its decoherence within 15 fs, and its revival after 40–50 fs. In addition, with the advancement of attosecond XUV pulse generation technology, its energy spectrum can now cover the *K*-edge of carbon atoms (roughly in the range of 260–300 eV), significantly broadening the applications of ATAS in organic molecules. A joint experimental and theoretical study on ATAS at the carbon *K*-edge in ethylene cation ($C_2H_4^+$)[110] revealed that the electronic relaxation of a core-excited state back to the ground state due to the coupled electronic and nuclear dynamics occurring at the CI can take place within a single period of the C=C stretch vibrational mode. A recent breakthrough on ATAS at the carbon *K*-edge in both isolated pyrazine molecules and those in aqueous solution[111] explored the impact of solvation on the conical intersection dynamics, revealing that solvation can dephase the dynamics within 40 fs and shorten its relaxation time.

5. ATAS in solids

When many atoms are arranged in a long-range order to form a crystal, complex many-body correlation emerges. From the perspective of real space, the motion of electrons in a single Coulomb potential evolves into that in a periodic Coulomb potential. From the perspective of reciprocal space, the energy levels of individual isolated atoms evolve into a shared energy band for all atoms. One of the most fascinating fundamental phenomena in solid-state physics is the light-driven motion and light excitation of electrons from the valence band (VB) to the conduction band (CB). In the time domain, the ultrafast laser-excited charge carrier dynamics are governed by different physical processes at different time scales. Roughly speaking, on the attosecond timescale, coherent electron dynamics are predominant. Within a few- to hundred-femtosecond range, electron–electron scattering processes become non-negligible. As the timescale extends from hundreds of femtoseconds to several picoseconds, electron spin–orbital coupling begins to play an evident role. Furthermore, in the temporal domain spanning from several picoseconds to tens of picoseconds, electron–phonon coupling emerges as a crucial process in the system's evolution.

5.1. Charge carrier dynamics in solids

The charge carrier dynamics have been extensively studied on time scales ranging from tens of femtoseconds to microseconds. Through time-resolved experiments, significant insights have been gained into processes such as carrier transport, electron–hole recombination, and exciton effects following the ultrafast laser-excitation.[113] However, it is still unclear how the electrons behave during the early and intermediate stages of the excitation process, especially when the strong field leads to a high number density of excited electrons. Disentangling the coupling dynamics between electrons (carrier–carrier scattering) and/or between electrons and lattice (carrier–phonon scattering) has long been a goal for condensed matter physicists until the advent of attosecond

lasers, as better understanding and distinction of those are a prerequisite for the material engineering and manipulation. The broadband attosecond x-ray laser generated by HHG offers a finer temporal and spectral resolution, covering core-to-valence transitions with element-specificity. These features enable the extraction of coherent attosecond charge dynamics underlying the complex many-body physics in solids, that is, allow for tracking the electron dynamics on the attosecond time scale, and then manipulate them in an optical manner. In this context, the ATAS is a powerful and widely used experimental technique. For example, in 2013, Schultze *et al.* extended the ATAS to a solid sample, investigating the sub-fs carrier dynamics in SiO_2.[114] In the next year, Schultze *et al.* used the same scheme to examine the carrier injection mechanism in Si.[115] From the delay-dependent absorption traces obtained through ATAS, they were able to distinguish the role of carrier–carrier interaction and electron–phonon coupling which occur on two different time scales of around 450 as and 60±10 fs, respectively.

At present, the research outcomes of ATAS in solids are becoming increasingly rich. From the perspective of electron–electron interaction, the ultrafast dynamics of electrons can be divided into three categories: (1) completely ignoring electron–electron interaction, (2) considering electron–electron interaction in the mean-field approximation, and (3) accounting for electron–electron interaction from first principles. Here, we primarily discuss the first two, using the single-active-electron behavior to represent the collective behavior. Additionally, the pump intensity range involved here is below the sample's laser-induced damage threshold, typically in the range of 10^{11} to several 10^{12} W/cm^2 where the dipole approximation holds and the interaction with the magnetic field of the laser can be completely ignored.[116,117]

The optical absorption of solids in strong laser fields can be understood from both real-space and reciprocal-space pictures. The real-space picture is based on Bloch oscillations and Wannier–Stark ladders widely mentioned in the literature (see Ref. [118] and references therein). ATAS, with its elemental specificity and the energy-scale separation between the IR pump and the XUV probe, ensures that the probe does not interfere with the pump-induced process. Additionally, the probe is capable of detecting the core-to-valence transition, particularly suitable for resolving the electron motion modulated by the pump from the reciprocal-space energy bands. In view of this, we will focus mainly on the reciprocal-space picture.

In the reciprocal-space picture, the ultrafast electron dynamics can be divided into interband transition and intraband motion. The former can be characterized by the Keldysh parameter similar to the strong-field ionization of an atom. In solids, within the parabolic band approximation, the Keldysh parameter is given by

$$\gamma_{\mathrm{K}} = \sqrt{\frac{E_{\mathrm{g}}}{4U_{\mathrm{p}}}}, \tag{14}$$

with the ponderomotive energy

$$U_{\mathrm{p}} = \frac{(e\mathcal{E}_0)^2(1+\beta^2)}{4m_{\mathrm{r}}\omega_{\mathrm{IR}}^2}, \tag{15}$$

where e is the electron charge, ω_{IR} is the pump photon energy, $\mathcal{E}_0$ is the pump field amplitude, m_{r} is the reduced electron–hole mass, E_{g} is the band gap, and β is the optical polarization ellipticity (which is zero for linear polarization). When $\gamma_{\mathrm{K}} \ll 1$, the interaction with the field is in the quasi-static limit, or equivalently, in the adiabatic tunneling regime. For $\gamma_{\mathrm{K}} \gg 1$, the multiphoton absorption becomes the dominant mechanism.

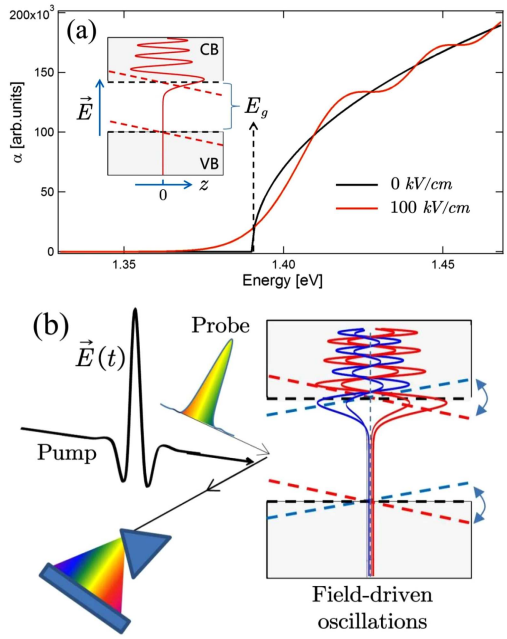


Fig. 9. Schematic description of the static (a) and dynamical (b) FKE and the associated main features observable in absorption spectrum. Adapted from Ref. [112].

The fundamental processes dominated by interband transition or intraband motion exhibit distinct features in the ATA spectrogram, which can be characterized by an adiabatic parameter

$$\gamma_{\mathrm{a}} = \frac{U_{\mathrm{p}}}{\hbar\omega_{\mathrm{IR}}}. \tag{16}$$

It describes an interplay between field-driven inter- and intraband dynamics. When $\gamma_{\mathrm{a}} \gg 1$, the external light field behaves as a quasi-static classical field in time and the Franz–Keldysh effect (FKE) related to intraband motion dominates the fundamental process. The external field bends the crystal potential, accelerating the electron–hole pair. In general, FKE has the following features in the absorption spectrum as illustrated in Fig. 9. (1) The existence of an exponentially decaying tail of the wavefunction below the bandgap resulting in optical absorption of $\hbar\omega < E_{\mathrm{g}}$. (2) The blue shift of the absorption edge

equal to U_p. (3) The oscillating absorption above the bandgap as a function of ω. Due to the feature (1), FKE is also referred to as photon-assisted tunneling. The case of $\gamma_a \sim 1$ is called dynamical FKE (DFKE), which is an ultrafast nonresonant process with no real carrier generation. The change of all the above FKE features in time following the external field waveform is characteristic of DFKE, which cannot be observed in the ATA spectrograms at low pump laser intensities. For $\gamma_a \ll 1$, the field shows its quantum nature, and the induced change of absorption is due to multiphoton processes.

We first discuss the case of $\hbar\omega_{IR} \ll E_g$. In 2016, Keller's group conducted a joint study of ATAS experiments and *ab initio* calculations on a 50-nm-thick polycrystalline diamond sample ($E_g = 5.5$ eV), which showed that the observed DFKE on the transient spectrum is caused by the intraband motion of virtual charge carriers.[119] When $\hbar\omega_{IR} \ll E_g$, the influence of interband transition by Zener-type tunneling can be avoided, facilitating the resolution of pure DFKE. Specifically, they used a 250-as XUV pulse (center energy $\hbar\omega_{XUV} \sim 42$ eV) to probe the optical response of VB to CB subbands to few-fs NIR (center energy $\hbar\omega_{IR} = 1.58$ eV) pulses. Note that the XUV transition here is from VB to CB not requiring the core-band participation, so that a two-band model that includes only the VB and CB seems to well reproduce the experimental observations. A V-shaped structure that oscillates with $2\omega_{IR}$, localized in the pump–probe overlap region, was revealed by the ATAS data [Fig. 10(a)], both theoretically and experimentally. This was identified as a fingerprint of DFKE, which later became known as "fishbone structure". The same group repeated the experiment using the same sample and a very similar methodology and setup to study the attosecond optical response to 800-nm IR pulses with an intensity range of $1.4–10.5 \times 10^{12}$ W/cm^2 corresponding to $0.04 < \gamma_a < 0.3$.[120] Special attention was paid to the precise timing between the energy-dependent transient absorption modulations and the pump field, or equivalently, the tilt angle of the fishbone structure. It was found that, for small γ_a and at the fishbone apex (43 eV), the main oscillation feature that reflects the phase delay or timing is qualitatively unaffected by the variation of the pump intensity within the experimental uncertainty. Otobe *et al.* from Japan developed a set of analytical theories for DFKE based on the two-parabolic-band approximation, applying it to a bulk diamond ($E_g = 5.6$ eV significantly greater than $\omega_{IR} = 0.4$ eV) to demonstrate the DFKE.[121] The γ_a range studied was from 0.29 to 29.5 within which, however, the phase delay at the main oscillation feature varied significantly with the change of pump intensity. More recently, this theoretical formalism was again used to explain the fishbone structure of DFKE.[122] It is shown that the fishbone apex appeared at U_p above the band gap and the V-shape structure originates from the mixing of the real and imaginary parts of the third-order susceptibility.

Next is the case of $\hbar\omega_{IR} \gg E_g$, as studied by Volkov *et al.* in 2019.[123] They used a 1.55 eV IR pulse with a peak intensity of $7.5\pm0.7\times10^{11}$ W/cm^2 to excite a transition metal film (Ti, $E_g = 0.23$ eV at the Γ and A points), providing a state-resolved (achieved through TDDFT) and attosecond time-resolved (achieved through ATAS) view of the few-fs electron dynamics. Unlike the mechanisms in wide-bandgap materials, where pump-induced intraband and interband transitions modulate transient absorption, the optical response of Ti is attributed to ultrafast electron localization induced by the IR-pump pulse, which alters atomic dielectric screening and results in step-like changes in absorption [Fig. 10(b)]. They also observed identical spectral features at the $N_{2,3}$ absorption edge of zirconium, suggesting that this phenomenon is universal for transition metals.

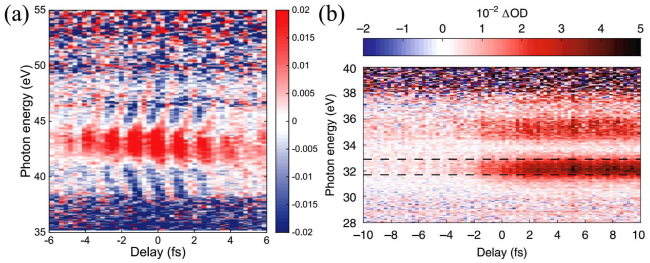


Fig. 10. Distinctive characteristics observed in the ATA spectrograms of a dielectric (a), e.g., polycrystalline diamond, and a metal (b), e.g., Ti. They fall into two different regions, $\hbar\omega_{IR} \ll E_g$ and $\hbar\omega_{IR} \gg E_g$, respectively. As a result, a typical fishbone structure was observed in the former while a step-like absorption was found for the latter. Adapted from Refs. [119,123]. Both are experimental data.

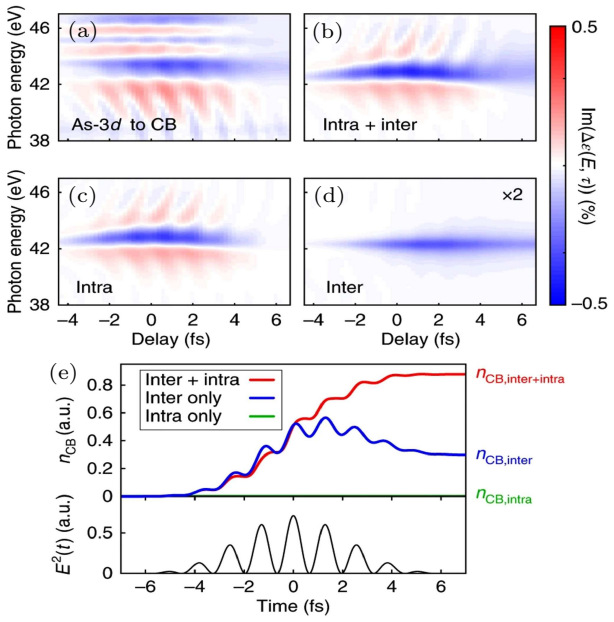


Fig. 11. *Ab-initio* simulation of ATAS in bulk GaAs (a), a typical semiconductor, along with the identification of the separated contributions from the intraband motion and interband transition based on a simplified three-band model (b)–(e). The ATA spectrogram possesses the combined features of an insulator and a metal. See also Fig. 10 for comparison. Adapted from Ref. [124].

Last but not least, we discuss the primary carrier injection mechanism when $\hbar\omega_{\rm IR} \sim E_{\rm g}$. In 2018, Keller's group extended their previous research[119] by discussing the combined effects of interband and intraband motions on the transient optical response,[124] using a GaAs membrane ($E_{\rm g} = 1.42$ eV at room temperature) and an IR-photon energy of 1.59 eV. With the help of a three-band model, they were able to distinguish the contributions from intraband motion and interband transition in the ATA spectrogram (Fig. 11). The authors found that intraband motion can significantly enhance the carrier injection from the VB to CB. Although the intraband motion itself contributed by virtual carriers cannot create the real carriers in CB, its facilitative role in the carrier injection process is substantial, as shown in Fig. 11(e). This physical phenomenon can be utilized to control the ultrafast carrier excitation and improve the ultrafast optical switching rate in the PHz regime.

How fast can a solid respond to the ultrafast laser field? — As discussed earlier for $\hbar\omega_{\rm IR} \gg E_{\rm g}$, the phase delay between the fishbone apex and the optical field extremum varies with laser field parameters, which is akin to the buildup time in atomic ATAS. Figures 12(a) and 12(b) display the ATA spectrograms predicted according to the DFKE theory, illustrating the increasing tilt angle of the fishbone structure as $\gamma_{\rm a}$ transitions from the non-adiabatic to the adiabatic regime. In the fully adiabatic case [Fig. 12(c)], i.e., assuming an instantaneous response to the pump laser field, the tilt angle reaches 90°. This implies a gradual transition from non-instantaneous to instantaneous response, indicating that the phase delay extracted from ATA spectrograms can reflect the solid's response time to the external field. However, the precise mapping between the two quantities remains to be further explored. Figure 12(d) shows the delay-integrated results from panels (a)–(c). Notably, the curve for $\gamma_{\rm a} \gg 1$ nearly coincides with that for the static FKE (black dashed line), while significant deviations are observed for $\gamma_{\rm a} \ll 1$.

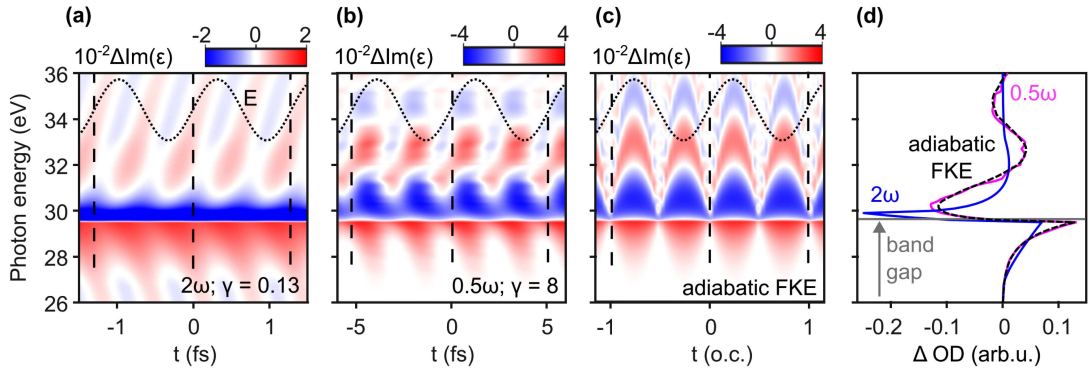


Fig. 12. The tilt angle of the fishbone structure increases as the laser parameters switch from the nonadiabatic regime (a) to the adiabatic regime (b), and reaches the maximum (90°) when assuming an instantaneous response to the pump laser electric field (c). Therefore, the tilt angle signifies the adiabaticity of the system and even quantifies the response time of a certain material to the external laser field. Panel (d) shows that the cycle-averaged ATAS spectrum in the adiabatic regime (solid magenta line) recovers the conventional, static-FKE electroabsorption spectrum (black dashed line). Adapted from Ref. [122].

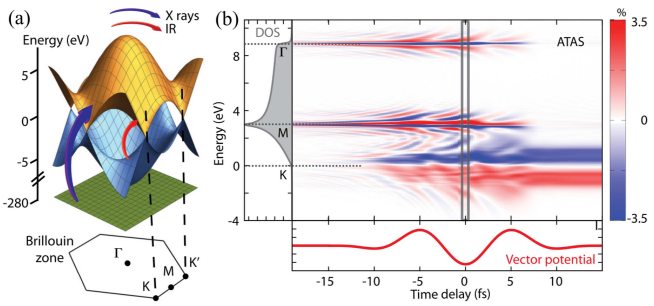


Fig. 13. Energy band structure of the graphene (a) and the predicted ATA spectrogram (b). The Fermi level is set to the zero of energy. Adapted from Ref. [46].

In condensed matter physics, the energy band structure of materials is highly variable. Due to the theoretical convenience of obtaining analytical or semi-analytical solutions for parabolic bands, extensive theoretical and experimental studies have been conducted on materials with such band structure in the context of ATAS. Recently, research has begun to expand to two-dimensional materials with Dirac cone-like band dispersion relations, such as graphene. Figure 13 presents the ATAS in graphene, revealing that the spectral features at the Γ and M points, characterized by parabolic dispersion, are consistent with prior results. In contrast, the spectral features at the Dirac point (K point), which exhibits linear dispersion, display notable differences. Whether this linear dispersion can significantly reduce the response time, thereby advancing the development of ultrafast optoelectronics (see Subsection 5.2), could be an interesting topic for further investigation.

5.2. Applications in PHz electronics

Traditional digital electronics based on large-scale integrated circuits rely on alternating current generated by semiconductor heterojunctions and transistors to switch states (ON and OFF). The switching speed of the fastest semiconductor transistor can reach 800 GHz under the condition of the sample temperature equal to 4.3 K.[125] As the chip size decreases,

traditional electronics technology has encountered bottlenecks due to the limitation of quantum effects. The switching speed of the digital electronic device is difficult to exceed 1 THz, and the corresponding response speed of the electric switch is limited to 1 ps. The development of ultrafast optical switching has broken through this limitation and opened the door to ultrafast electronics, i.e., PHz electronics.

In 2013, based on the $2\omega_{\mathrm{IR}}$ oscillation feature of CB occupancy in the pump–probe overlap region revealed by the ATA spectrogram of the SiO_2 film, Schultze *et al.* found that as long as the material is not broken down, the pump field-induced changes of all the studied physical quantities, such as CB population, dielectric polarization, are reversible, following the field waveform.[114] In other words, these quantities can be turned on and off on the time scale of optical cycles, allowing the real-time observation and control of strong field phenomena in dielectrics on the sub-fs to few-fs time scales. In the following year, an ATAS study at $L_{2,3}$ edge of semiconductor Si (direct bandgap is about 3.2 eV) also revealed this mechanism.[115] The above researches demonstrated the ultrafast control of carrier motion induced by an intense laser field in the tunneling regime of $\gamma_{\mathrm{K}} < 1$. In contrast, carrier injection into the CB through multiphoton absorption ($\gamma_{\mathrm{K}} \gg 1$) can also enable PHz carrier manipulation. Mashiko *et al.* observed $3\omega_{\mathrm{IR}}$ ($= 1.16$ PHz) and $7\omega_{\mathrm{IR}}$ ($= 2.6$ PHz) absorption trace oscillations in their ATAS experiments on gallium nitride (GaN) ($E_{\mathrm{g}} \approx 3.4$ eV),[45] a direct-gap semiconductor, and Cr:Al_2O_3 ($E_{\mathrm{g}} = 5$ eV),[126] a wide bandgap insulator Al_2O_3 doped with Cr ions, respectively. The latter, in particular, shows that it is possible to manipulate carriers in the dielectric at a rate of multi-PHz with frequency tunability offered by choosing the identity of the chemical dopant. The above examples highlight the huge potential of ATAS in PHz electronics and high-speed signal processing based on wide-bandgap semiconductors.

When switching, semiconductor transistors dissipate all stored energy through the electron–hole recombination. In contrast, attosecond optical switching generates minimal dissipation and is more energy-efficient, as dielectrics return nearly all stored energy to the pump field. Reference [127] outlined the physical requirements for achieving the PHz-speed device utilizing solid materials with parabolic energy bands: a wide bandgap, a first conduction band with large bandwidth, and weak coupling between the first CB and higher CBs, and predicted that the response speed limit for such PHz electronic devices is approximately 1 PHz.

6. Conclusions

Attosecond transient absorption spectroscopy has emerged as a powerful tool for studying ultrafast electronic dynamics across various systems, from atoms to solids. The extremely short duration of attosecond pulses provides an excellent temporal reference point (delay zero). Moreover, the ability to precisely control the relative time delay between two light pulses at the attosecond time precision offers a fine-tuned "clock" that allows for unprecedented accuracy in observing material behavior on the natural timescale of electron motion.

In atoms, ATAS has been instrumental in studying the build-up dynamics of Autler–Townes splitting, Fano resonance, and light-induced states. The technique has provided detailed insights into the coherent electronic dynamics of atoms imprinted in sub-laser-cycle quantum beats. The ability to track or even reconstruct the real-time response of atoms to external fields has opened new avenues for understanding the fundamental electronic processes. In molecules, ATAS has revealed coherent molecular wavepacket dynamics and nonadiabatic dynamics near conical intersections. The technique has enabled the observation and manipulation of coherent dynamics of molecular wavepackets, providing detailed insights into the ultrafast dynamics of electronic, vibrational, and rotational states. In solids, ATAS has been extended to investigate ultrafast charge carrier dynamics in metals, semiconductors, and insulators. The technique has provided detailed insights into the coherent electron dynamics in solids, such as the dynamical Franz–Keldysh effect. The ability to track the ultrafast dynamics of charge carriers in solids has opened new possibilities for developing ultrafast optical switches and petahertz electronics. Overall, ATAS has demonstrated significant potential in probing and manipulating electronic dynamics at the attosecond timescale. Its applications have spanned from fundamental research to potential technological advancements.

ATAS holds much more exciting possibilities with the continued shortening of attosecond pulses and enhancement of photon flux. Thanks to the advancements in table-top high-order harmonics generation and seeded free electron lasers, broadband x-ray capable of covering the water window has now become available,[128] enabling simultaneous probing of the absorption edges of carbon, nitrogen, and oxygen. Very recently, the first ATA spectrogram in liquid water was achieved through attosecond-pump attosecond-probe x-ray spectroscopy.[129] ATAS in the water window is highly anticipated for ultrafast studies of biological and chemical reactions in solvent environments, heralding a promising direction for future research. Developing other ATAS-complementing solid-state techniques, such as attosecond transient reflection spectroscopy, offers another exciting avenue.[130] ATRS is less sensitive to sample thickness, overcoming the limitations of ATAS and making it ideal for probing bulk samples and studying interface chemistry. By controlling the polarization of attosecond pulses, researchers can also study magnetic circular dichroism effects in ultrafast magnetism.[131] Furthermore, the application of ATAS to low-dimensional materials,[132] topo-

logical insulators,[133] and strongly correlated electron systems like superconductors,[134] is expected to provide new insights into the unique electronic properties of these materials. The future of ATAS is limited only by our imagination.

Acknowledgement

Project supported by the National Natural Science Foundation of China (Grant No. 12174034).

References

[1] Strickland D and Mourou G 1985 *Opt. Commun.* **56** 219
[2] Mourou G 2019 *Rev. Mod. Phys.* **91** 030501
[3] Strickland D 2019 *Rev. Mod. Phys.* **91** 030502
[4] Paul P M, Toma E S, Breger P, Mullot G, Augé F, Balcou Ph, Muller H G and Agostini P 2001 *Science* **292** 1689
[5] Hentschel M, Kienberger R, Spielmann Ch, Reider G A, Milosevic N, Brabec T, Corkum P, Heinzmann U, Drescher M and Krausz F 2001 *Nature* **414** 509
[6] Krausz F and Ivanov M 2009 *Rev. Mod. Phys.* **81** 163
[7] Agostini P 2024 *Rev. Mod. Phys.* **96** 030501
[8] Krausz F 2024 *Rev. Mod. Phys.* **96** 030502
[9] L'Huillier A 2024 *Rev. Mod. Phys.* **96** 030503
[10] Gallmann L, Herrmann J, Locher R, Sabbar M, Ludwig A, Lucchini M and Keller U 2013 *Mol. Phys.* **111** 2243
[11] Wu M, Chen S, Camp S, Schafer K J and Gaarde M B 2016 *J. Phys. B: At. Mol. Opt. Phys.* **49** 062003
[12] Geneaux R, Marroux H J B, Guggenmos A, Neumark D M and Leone S R 2019 *Phil. Trans. R. Soc. A* **377** 20170463
[13] Palacios A and Martín F 2020 *WIREs Comput. Mol. Sci.* **10** e1430
[14] Biegert J, Calegari F, Dudovich N, Quéré F and Vrakking M 2021 *J. Phys. B: At. Mol. Opt. Phys.* **54** 070201
[15] Borrego-Varillas R, Lucchini M and Nisoli M 2022 *Rep. Prog. Phys.* **85** 066401
[16] Hu S and Meng S 2023 *Chin. Phys. Lett.* **40** 117801
[17] Zong A, Nebgen B R, Lin S C, Spies J A and Zuerch M 2023 *Nat. Rev. Mater.* **8** 224
[18] Di Palo N, Inzani G, Dolso G L, Talarico M, Bonetti S and Lucchini M 2024 *APL Photonics* **9** 020901
[19] Gaarde M B, Buth C, Tate J L and Schafer K J 2011 *Phys. Rev. A* **83** 013419
[20] Stenquist A, Zapata F and Dahlström J M 2023 *Phys. Rev. A* **107** 053106
[21] Argenti L, Jiménez-Galán Á, Marante C, Ott C, Pfeifer T and Martín F 2015 *Phys. Rev. A* **91** 061403
[22] Petersson C L M, Argenti L and Martín F 2017 *Phys. Rev. A* **96** 013403
[23] Colgan J, Pindzola M S and Robicheaux F 2004 *Phys. Rev. Lett.* **93** 053201
[24] Colgan J and Pindzola M S 2012 *Phys. Rev. Lett.* **108** 053001
[25] Colgan J, Emmanouilidou A and Pindzola M S 2013 *Phys. Rev. Lett.* **110** 063001
[26] Bækhøj J E, Yue L and Madsen L B 2015 *Phys. Rev. A* **91** 043408
[27] Chen S, Wu M, Gaarde M B and Schafer K J 2013 *Phys. Rev. A* **87** 033408
[28] Murakami M and Chu S I 2013 *Phys. Rev. A* **88** 043428
[29] Chini M, Wang X, Cheng Y and Chang Z 2014 *J. Phys. B: At. Mol. Opt. Phys.* **47** 124009
[30] Dong W, Li Y, Wang X, Yuan J and Zhao Z 2015 *Phys. Rev. A* **92** 033412
[31] Zhao H, Liu C, Zheng Y, Zeng Z and Li R 2017 *Opt. Express* **25** 7707
[32] Yuan G, Jiang S, Wang Z, Hua W, Yu C, Jin C and Lu R 2019 *Struct. Dyn.* **6** 054102
[33] Chu W C and Lin C D 2010 *Phys. Rev. A* **82** 053415
[34] Chu W C, Zhao S F and Lin C D 2011 *Phys. Rev. A* **84** 033426
[35] Pfeiffer A N and Leone S R 2012 *Phys. Rev. A* **85** 053422
[36] Wu M, Chen S, Gaarde M B and Schafer K J 2013 *Phys. Rev. A* **88** 043416
[37] Mi K, Cao W, Xu H, Mo Y, Yang Z, Lan P, Zhang Q and Lu P 2020 *Phys. Rev. Appl.* **13** 014032
[38] He Y, Liu Z, Ott C, Pfeiffer A N, Sun S, Gaarde M B, Pfeifer T and Hu B 2022 *Phys. Rev. Lett.* **129** 273201
[39] Fu Y, Wang B, Wang K, Tang X, Li B, Yin Z, Han J, Lin C D and Jin C 2024 *Proc. Natl. Acad. Sci. USA* **121** e2307836121
[40] Vrakking M J J and Lepine F 2018 *Attosecond Molecular Dynamics* (Cambridge: The Royal Society of Chemistry)
[41] Wang H, Odelius M and Prendergast D 2019 *J. Chem. Phys.* **151** 124106
[42] Zettergren H, Domaracka A, Schlathölter T, *et al.* 2021 *Eur. Phys. J. D* **75** 152
[43] Alexander O G, Marangos J P, Ruberti M and Vacher M 2023 *Advances In Atomic, Molecular, and Optical Physics* vol. 72, Ed. by L F DiMauro, H Perrin and S F Yelin (Academic Press) pp. 183—251
[44] Casperson L W 1998 *Phys. Rev. A* **57** 609
[45] Mashiko H, Oguri K, Yamaguchi T, Suda A and Gotoh H 2016 *Nat. Phys.* **12** 741
[46] Cistaro G, Plaja L, Martín F and Picón A 2021 *Phys. Rev. Res.* **3** 013144
[47] Cavaletto S M and Madsen L B 2024 *Phys. Rev. A* **110** 053111
[48] Cavaletto S M, Kowalczyk K M, Navarrete F O and Rivera-Dean J 2025 *Nat. Rev. Phys.* **7** 38
[49] Dong F and Liu J 2022 *Phys. Rev. A* **106** 063107
[50] Castro A, Marques M A L and Rubio A 2004 *J. Chem. Phys.* **121** 3425
[51] Andrade X, Strubbe D, De Giovannini U, Larsen A H, Oliveira M J T, Alberdi-Rodriguez J, Varas A, Theophilou I, Helbig N, Verstraete M J, Stella L, Nogueira F, Aspuru-Guzik A, Castro A, Marques M A L and Rubio A 2015 *Phys. Chem. Chem. Phys.* **17** 31371
[52] Tong X M and Chu S I 2001 *Phys. Rev. A* **64** 013417
[53] Otobe T, Yabana K and Iwata J I 2004 *Phys. Rev. A* **69** 053404
[54] Gao C Z, Dinh P M, Reinhard P G and Suraud E 2017 *Phys. Chem. Chem. Phys.* **19** 19784
[55] Moitra T, Konecny L, Kadek M, Rubio A and Repisky M 2023 *J. Phys. Chem. Lett.* **14** 1714
[56] Chen M and Lopata K 2020 *J. Chem. Theory Comput.* **16** 4470
[57] Sato S A, Hübener H, De Giovannini U and Rubio A 2018 *Appl. Sci.* **8** 1777
[58] Boolakee T, Heide C, Garzón-Ramírez A, Weber H B, Franco I and Hommelhoff P 2022 *Nature* **605** 251
[59] Pfeiffer A N, Bell M J, Beck A R, Mashiko H, Neumark D M and Leone S R 2013 *Phys. Rev. A* **88** 051402
[60] Lin C D, Le A T, Jin C and Wei H 2018 *Attosecond and Strong-Field Physics: Principles and Applications* (Cambridge: Cambridge University Press)
[61] Santra R, Yakovlev V S, Pfeifer T and Loh Z H 2011 *Phys. Rev. A* **83** 033405
[62] Goulielmakis E, Loh Z H, Wirth A, Santra R, Rohringer N, Yakovlev V S, Zherebtsov S, Pfeifer T, Azzeer A M, Kling M F, Leone S R and Krausz F 2010 *Nature* **466** 739
[63] Wang H, Chini M, Chen S, Zhang C H, He F, Cheng Y, Wu Y, Thumm U and Chang Z 2010 *Phys. Rev. Lett.* **105** 143002
[64] Holler M, Schapper F, Gallmann L and Keller U 2011 *Phys. Rev. Lett.* **106** 123601
[65] Ott C, Kaldun A, Argenti L, Raith P, Meyer K, Laux M, Zhang Y, Blättermann A, Hagstotz S, Ding T, Heck R, Madroñero J, Martín F and Pfeifer T 2014 *Nature* **516** 374
[66] Chini M, Wang X, Cheng Y, Wu Y, Zhao D, Telnov D A, Chu S I and Chang Z 2013 *Sci. Rep.* **3** 1105
[67] Yang Z Q, Ye D F, Ding T, Pfeifer T and Fu L B 2015 *Phys. Rev. A* **91** 013414
[68] Sabbar M, Timmers H, Chen Y J, Pymer A K, Loh Z H, Sayres S G, Pabst S, Santra R and Leone S R 2017 *Nat. Phys.* **13** 472
[69] Wang L, Bai G, Wang X, Zhao J, Gao C, Wang J, Xiao F, Tao W, Song P, Qiu Q, Liu J and Zhao Z 2024 *Nat. Commun.* **15** 2705
[70] Lindberg M and Koch S W 1988 *Phys. Rev. B* **38** 7607
[71] Yan S, Seidel M T and Tan H S 2011 *Chem. Phys. Lett.* **517** 36
[72] Wang X, Chini M, Cheng Y, Wu Y, Tong X M and Chang Z 2013 *Phys. Rev. A* **87** 063413
[73] Wu X, Yang Z, Zhang S, Ma X, Liu J and Ye D 2021 *Phys. Rev. A* **103** L061102
[74] Xie Q, Zhong H, Batchelor M T and Lee C 2017 *J. Phys. A: Math. Theor.* **50** 113001
[75] Reduzzi M, Hummert J, Dubrouil A, Calegari F, Nisoli M, Frassetto F, Poletto L, Chen S, Wu M, Gaarde M B, Schafer K and Sansone G 2015 *Phys. Rev. A* **92** 033408

[76] Becker P C, Fork R L, Brito Cruz C H, Gordon J P and Shank C V 1988 *Phys. Rev. Lett.* **60** 2462
[77] Wu X, Zhang S and Ye D 2021 *J. Phys. B: At. Mol. Opt. Phys.* **54** 205602
[78] Chu W C and Lin C D 2012 *Phys. Rev. A* **85** 013409
[79] Chu W C and Lin C D 2013 *Phys. Rev. A* **87** 013415
[80] Anand M, Pabst S, Kwon O and Kim D E 2017 *Phys. Rev. A* **95** 053420
[81] Rørstad J J, Ravn N S W, Yue L and Madsen L B 2018 *Phys. Rev. A* **98** 053401
[82] Herrmann J, Lucchini M, Chen S, Wu M, Ludwig A, Kasmi L, Schafer K J, Gallmann L, Gaarde M B and Keller U 2015 *New J. Phys.* **17** 013007
[83] Géneaux R, Kaplan C J, Yue L, Ross A D, Bækhøj J E, Kraus P M, Chang H T, Guggenmos A, Huang M Y, Zürch M, Schafer K J, Neumark D M, Gaarde M B and Leone S R 2020 *Phys. Rev. Lett.* **124** 207401
[84] Jackson J D 1999 *Classical Electrodynamics*, 3rd edn. (New York: Wiley) pp. 330–339
[85] Boyd R W and Gauthier D J 2009 *Science* **326** 1074
[86] Leone S R, McCurdy C W, Burgdörfer J, Cederbaum L S, Chang Z, Dudovich N, Feist J, Greene C H, Ivanov M, Kienberger R, Keller U, Kling M F, Loh Z H, Pfeifer T, Pfeiffer A N, Santra R, Schafer K, Stolow A, Thumm U and Vrakking M J J 2014 *Nat. Photon.* **8** 162
[87] Sabbar M, Timmers H, Chen Y J, Pymer A K, Loh Z H, Sayres S G, Pabst S, Santra R and Leone S R 2017 *Nat. Phys.* **13** 472
[88] Peng P, Marceau C, Hervé M, Corkum P B, Naumov A Yu and Villeneuve D M 2019 *Nat. Commun.* **10** 5269
[89] Tsen K T 2004 *Ultrafast Dynamical Processes in Semiconductors*, (Heidelberg: Springer Berlin) pp. 10–13
[90] Zewail A H 1988 *Science* **242** 1645
[91] Pestov D, Murawski R K, Ariunbold G O, Wang X, Zhi M, Sokolov A V, Sautenkov V A, Rostovtsev Y V, Dogariu A, Huang Y and Scully M O 2007 *Science* **316** 265
[92] Yang Y, Yang M, Zhu K, Johnson J C, Berry J J, van de Lagemaat J and Beard M C 2016 *Nat. Commun.* **7** 12613
[93] Siegrist F, Gessner J A, Ossiander M, Denker C, Chang Y P, Schröder M C, Guggenmos A, Cui Y, Walowski J, Martens U, Dewhurst J K, Kleineberg U, Münzenberg M, Sharma S and Schultze M 2019 *Nature* **571** 240
[94] Li X, Bernhardt B, Beck A R, Warrick E R, Pfeiffer A N, Justine Bell M, Haxton D J, McCurdy C W, Neumark D M and Leone S R 2015 *J. Phys. B: At. Mol. Opt. Phys.* **48** 125601
[95] Ott C, Kaldun A, Raith P, Meyer K, Laux M, Evers J, Keitel C H, Greene C H and Pfeifer T 2013 *Science* **340** 716
[96] Blättermann A, Ott C, Kaldun A, Ding T and Pfeifer T 2014 *J. Phys. B: At. Mol. Opt. Phys.* **47** 124008
[97] Stooß V, Cavaletto S M, Donsa S, Blättermann A, Birk P, Keitel C H, Březinová I, Burgdörfer J, Ott C and Pfeifer T 2018 *Phys. Rev. Lett.* **121** 173005
[98] Wu X, Zhang L, Zhang S and Ye D 2021 *Phys. Rev. A* **104** 063121
[99] Heldt T, Dubois J, Birk P, Borisova G D, Lando G M, Ott C and Pfeifer T 2023 *Phys. Rev. Lett.* **130** 183201
[100] Cheng Y, Chini M, Wang X, González-Castrillo A, Palacios A, Argenti L, Martín F and Chang Z 2016 *Phys. Rev. A* **94** 023403
[101] Saito N, Sannohe H, Ishii N, Kanai T, Kosugi N, Wu Y, Chew A, Han S, Chang Z and Itatani J 2019 *Optica* **6** 1542
[102] Poullain S M, Kobayashi Y, Chang K F and Leone S R 2021 *Phys. Rev. A* **104** 022817
[103] Bækhøj J E, Lévêque C and Madsen L B 2018 *Phys. Rev. Lett.* **121** 023203
[104] Kobayashi Y, Chang K F, Zeng T, Neumark D M and Leone S R 2019 *Science* **365** 79
[105] Timmers H, Zhu X, Li Z, Kobayashi Y, Sabbar M, Hollstein M, Reduzzi M, Martínez T J, Neumark D M and Leone S R 2019 *Nat. Commun.* **10** 3133
[106] Chang K F, Reduzzi M, Wang H, Poullain S M, Kobayashi Y, Barreau L, Prendergast D, Neumark D M and Leone S R 2020 *Nat. Commun.* **11** 4042
[107] Chang K F, Wang H, Poullain S M, Prendergast D, Neumark D M and Leone S R 2021 *J. Chem. Phys.* **154** 234301
[108] Chang K F, Wang H, Poullain S M, González-Vázquez J, Bañares L, Prendergast D, Neumark D M and Leone S R 2022 *J. Chem. Phys.* **156** 114304
[109] Matselyukh D T, Despré V, Golubev N V, Kuleff A I and Wörner H J 2022 *Nat. Phys.* **18** 1206
[110] Zinchenko K S, Ardana-Lamas F, Seidu I, Neville S P, van der Veen J, Lanfaloni V U, Schuurman M S and Wörner H J 2021 *Science* **371** 489
[111] Chang Y P, Balciunas T, Yin Z, Sapunar M, Tenorio B N C, Paul A C, Tsuru S, Koch H, Wolf J P, Coriani S and Wörner H J 2025 *Nat. Phys.* **21** 137
[112] Novelli F, Fausti D, Giusti F, Parmigiani F and Hoffmann M 2013 *Sci. Rep.* **3** 1227
[113] Shah J 1996 *Ultrafast Spectroscopy of Semiconductors and Semiconductor Nanostructures* (New York: Springer Berlin)
[114] Schultze M, Bothschafter E M, Sommer A, Holzner S, Schweinberger W, Fiess M, Hofstetter M, Kienberger R, Apalkov V, Yakovlev V S, Stockman M I and Krausz F 2013 *Nature* **493** 75
[115] Schultze M, Ramasesha K, Pemmaraju C D, Sato S A, Whitmore D, Gandman A, Prell J S, Borja L J, Prendergast D, Yabana K, Neumark D M and Leone S R 2014 *Science* **346** 1348
[116] Reiss H R 2008 *Phys. Rev. Lett.* **101** 043002
[117] Ludwig A, Maurer J, Mayer B W, Phillips C R, Gallmann L and Keller U 2014 *Phys. Rev. Lett.* **113** 243001
[118] Kruchinin S Yu, Krausz F and Yakovlev V S 2018 *Rev. Mod. Phys.* **90** 021002
[119] Lucchini M, Sato S A, Ludwig A, Herrmann J, Volkov M, Kasmi L, Shinohara Y, Yabana K, Gallmann L and Keller U 2016 *Science* **353** 916
[120] Lucchini M, Sato S A, Schlaepfer F, Yabana K, Gallmann L, Rubio A and Keller U 2020 *J. Phys. Photon.* **2** 025001
[121] Otobe T, Shinohara Y, Sato S A and Yabana K 2016 *Phys. Rev. B* **93** 045124
[122] Volkov M, Sato S A, Niedermayr A, Rubio A, Gallmann L and Keller U 2023 *Phys. Rev. B* **107** 184304
[123] Volkov M, Sato S A, Schlaepfer F, Kasmi L, Hartmann N, Lucchini M, Gallmann L, Rubio A and Keller U 2019 *Nat. Phys.* **15** 1145
[124] Schlaepfer F, Lucchini M, Sato S A, Volkov M, Kasmi L, Hartmann N, Rubio A, Gallmann L and Keller U 2018 *Nat. Phys.* **14** 560
[125] Chakraborty P S, Cardoso A S, Wier B R, Omprakash A P, Cressler J D, Kaynak M and Tillack B 2014 *IEEE Electron Device Lett.* **35** 151
[126] Mashiko H, Chisuga Y, Katayama I, Oguri K, Masuda H, Takeda J and Gotoh H 2018 *Nat. Commun.* **9** 1468
[127] Ossiander M, Golyari K, Scharl K, Lehnert L, Siegrist F, Bürger J P, Zimin D, Gessner J A, Weidman M, Floss I, Smejkal V, Donsa S, Lemell C, Libisch F, Karpowicz N, Burgdörfer J, Krausz F and Schultze M 2022 *Nat. Commun.* **13** 1620
[128] Zinchenko K S, Ardana-Lamas F, Lanfaloni V U, Luu T T, Pertot Y, Huppert M and Wörner H J 2023 *Sci. Rep.* **13** 3059
[129] Li S, Lu L, Bhattacharyya S, *et al.* 2024 *Science* **383** 1118
[130] Inzani G, Adamska L, Eskandari-asl A, Di Palo N, Dolso G L, Moio B, D'Onofrio L J, Lamperti A, Molle A, Borrego-Varillas R, Nisoli M, Pittalis S, Rozzi C A, Avella A and Lucchini M 2023 *Nat. Photon.* **17** 1059
[131] Siegrist F, Gessner J A, Ossiander M, Denker C, Chang Y P, Schröder M C, Guggenmos A, Cui Y, Walowski J, Martens U, Dewhurst J K, Kleineberg U, Münzenberg M, Sharma S and Schultze M 2019 *Nature* **571** 240
[132] Kim Y 2024 *npj Quantum Materials* **9** 86
[133] Mosquera J F P, Cistaro G, Malakhov M, Pisanty E, Dauphin A, Plaja L, Chacón A, Lewenstein M and Picón A 2024 *Rep. Prog. Phys.* **87** 117901
[134] Valmispild V N, Gorelov E, Eckstein M, Lichtenstein A I, Aoki H, Katsnelson M I, Ivanov M Y and Smirnova O 2023 *Nat. Photon.* **18** 432